On the Use of Advection Correction in Trajectory Calculations

ALAN SHAPIRO

School of Meteorology, and Center for Analysis and Prediction of Storms, University of Oklahoma, Norman, Oklahoma

STEFAN RAHIMI

Department of Atmospheric Science, University of Wyoming, Laramie, Wyoming

COREY K. POTVIN

Cooperative Institute for Mesoscale Meteorological Studies, and NOAA/OAR/National Severe Storms Laboratory, and School of Meteorology, University of Oklahoma, Norman, Oklahoma

LEIGH ORF

Central Michigan University, Mount Pleasant, Michigan

(Manuscript received 27 March 2015, in final form 8 July 2015)

ABSTRACT

An advection correction procedure is used to mitigate temporal interpolation errors in trajectory analyses constructed from gridded (in space and time) velocity data. The procedure is based on a technique introduced by Gal-Chen to reduce radar data analysis errors arising for the nonsimultaneity of the data collection. Experiments are conducted using data from a high-resolution Cloud Model 1 (CM1) numerical model simulation of a supercell storm initialized within an environment representative of the 24 May 2011 El Reno, Oklahoma, tornadic supercell storm. Trajectory analyses using advection correction are compared to traditional trajectory analyses using linear time interpolation. Backward trajectories are integrated over a 5-min period for a range of data input time intervals and for velocity-pattern-translation estimates obtained from different analysis subdomain sizes (box widths) and first-guess options. The use of advection correction reduces trajectory end-point position errors for a large majority of the trajectories in the analysis domain, with substantial improvements for trajectories launched in the vicinity of the model storm's gust front and in bands within the rear-flank downdraft. However, the pattern-translation components retrieved by this procedure may be nonunique if the data input time intervals are too large.

1. Introduction

The powerful tool of trajectory analysis has found widespread application in the environmental sciences. When coupled with vorticity and thermal energy budgets, trajectory analyses have provided insights into convective storm dynamics, including longstanding problems on the origins of low-level rotation in mesocyclones and tornadoes. Such analyses have been constructed from multiple-Doppler radar wind observations (Brandes 1981, 1984; Johnson et al. 1987; Wakimoto et al. 1998; Ziegler et al. 2001; Bluestein and Gaddy 2001; Dowell and Bluestein 2002; Marquis et al. 2008, 2012, 2014; Frame et al. 2009; Kosiba et al. 2013) and from numerically simulated storm data (Rotunno and Klemp 1985; Davies-Jones and Brooks 1993; Adlerman et al. 1999; Dawson et al. 2010; Dahl et al. 2012, 2014; Schenkman et al. 2012, 2014; Naylor and Gilmore 2014). Most recently, trajectory analyses have been applied to ensemble Kalman filter wind retrievals of supercell thunderstorms observed by mobile radar (Marquis et al. 2012, 2014; Potvin et al. 2013). Trajectories have been used to study atmospheric dispersion and to determine the source regions of pollutants (Stohl and Kromp-Kolb 1994; Stohl 1996, 1998; Brankov et al. 1998; Buchanan

Corresponding author address: Alan Shapiro, School of Meteorology, University of Oklahoma, 120 David L. Boren Blvd., Room 5900, Norman, OK 73072.
E-mail: ashapiro@ou.edu

DOI: 10.1175/JAS-D-15-0095.1

et al. 2002; Sturman and Zawar-Reza 2002; Park et al. 2007; Baker 2010) and of spores and pollen allergens (Hjelmroos 1991; Rantio-Lehtimäki 1994; Stach et al. 2007; Smith et al. 2008; Belmonte et al. 2008), pollen from genetically modified crops (Van de Water et al. 2007; Kuparinen et al. 2007; Beckie and Hall 2008), and pollen from illegal cultivations (Cabezudo et al. 1997). Trajectories are used in synoptic and climatological analyses to elucidate prevailing airflow patterns and associated pathways for the transport of water vapor, chemical species, and aerosols (Miller 1981; Dayan 1986; Moody et al. 1995; D'Abreton and Tyson 1996; Salathé and Hartmann 1997; Kahl et al. 1997; Wernli and Davies 1997; Shadboldt et al. 2006; Engelstaedter et al. 2006; Knippertz and Wernli 2010). They can also be used to analyze and forecast the spread of contaminants from environmental disasters such as nuclear reactor breaches (Pöllänen et al. 1997; Povinec et al. 2013; Ioannidou et al. 2013) and offshore oil spills (Spaulding 1988; Price et al. 2006; Sotillo et al. 2008; Liu et al. 2011; Xu et al. 2013). Other oceanographic applications include tracking floating mines and fish larvae, providing guidance for rescue and recovery operations, improving the analysis of oceanic circulations, and revealing the origin and destination of water masses (Blanke and Raynaud 1997; Griffa et al. 2004; Breivik and Allen 2008; Melsom et al. 2012; Chu and Fan 2014).

In most of these studies, parcel trajectories are constructed from gridded velocity data available on fixed grid points at equally spaced data (observation) times. The trajectories are computed as solutions of the ordinary differential equation,

$$\frac{D\mathbf{x}}{Dt} = \mathbf{u}(\mathbf{x}, t), \tag{1}$$

where $\mathbf{x} = \mathbf{x}(t, \mathbf{x}_0)$ is the parcel location at time t, $\mathbf{x}_0$ is the initial parcel location ($\mathbf{x}_0$ is a unique attribute of a parcel and can serve as the parcel name), D/Dt is the material (Lagrangian) derivative, and $\mathbf{u}(\mathbf{x}, t) = \mathbf{u}[\mathbf{x}(t, \mathbf{x}_0), t]$ is the velocity of the parcel at time t expressed in a hybrid Eulerian–Lagrangian notation.[1] Equation (1) is integrated over a set of computational times with a time step that is typically much smaller than the data input time interval. However, since the parcels invariably travel between the grid points, spatial and temporal interpolation steps are necessary at each computational time to estimate the parcel velocity $\mathbf{u}[\mathbf{x}(t, \mathbf{x}_0), t]$ from the gridded velocity data.

[1] Here we express the velocity of parcel $\mathbf{x}_0$ at time t as $\mathbf{u}[\mathbf{x}(t, \mathbf{x}_0), t]$, the value of the velocity field at time t at the location $\mathbf{x}(t, \mathbf{x}_0)$ occupied by parcel $\mathbf{x}_0$ at time t.

The utility of a trajectory analysis depends, in part, on the sensitivity and accuracy of the computed trajectories, various aspects of which have been discussed by Kuo et al. (1985), Kahl and Samson (1986), Rolph and Draxler (1990), Doty and Perkey (1993), Seibert (1993), Stohl et al. (1995, 2001), Scheele et al. (1996), Stohl (1998), Stohl and Seibert (1998), and Dahl et al. (2012). Among the major sources of trajectory error are truncation errors associated with the numerical integration scheme, spatial and temporal interpolation errors in the estimation of $\mathbf{u}[\mathbf{x}(t, \mathbf{x}_0), t]$ from the gridded velocity data, and errors in the gridded velocities arising, for example, from instrument errors (if observational data are used) or errors associated with model physics, initialization, and data assimilation (if data from a numerical prediction model are used). The focus of our study is the mitigation of errors stemming from just one of these sources: the time interpolation step.

Although a few trajectory models adopt a steady-state assumption or use quadratic interpolation, by far the most common time interpolation procedure is linear interpolation. In a comparison of the linear, quadratic, and nearest-neighbor (piecewise steady state) interpolation methods reported in Stohl et al. (1995), the nearest-neighbor approach yielded the largest errors, linear interpolation yielded the best results, and quadratic interpolation produced results that were similar to, but slightly worse than, linear interpolation. Rössler et al. (1992) also report only minor differences between uses of quadratic and linear interpolations. A common theme in the sensitivity/accuracy studies is that significant trajectory position errors can develop if the temporal resolution of the data is too coarse (Kuo et al. 1985; Rolph and Draxler 1990; Rössler et al. 1992; Doty and Perkey 1993; Stohl et al. 1995, 2001; Stohl 1998; Dahl et al. 2012). The establishment of criteria for minimal acceptable temporal resolutions does not appear to be straightforward; such resolutions appear to depend, in part, on the flow characteristics (Rolph and Draxler 1990; Stohl et al. 1995; Dahl et al. 2012).

In this study we explore the use of advection correction to mitigate errors in the time interpolation step. Advection correction is based on the Taylor (1938) hypothesis that, for sufficiently small time intervals, the velocity field can be idealized as a complex turbulent pattern that shifts horizontally (translates) without changing its form. This so-called frozen-turbulence hypothesis can be expressed in functional form as

$$u(x, y, t) = f(x - Ut, y - Vt) \quad \text{and} \tag{2a}$$

$$v(x, y, t) = g(x - Ut, y - Vt), \tag{2b}$$

or, equivalently, in differential form as

$$\frac{\partial u}{\partial t} + U\frac{\partial u}{\partial x} + V\frac{\partial u}{\partial y} = 0 \quad \text{and} \tag{3a}$$

$$\frac{\partial v}{\partial t} + U\frac{\partial v}{\partial x} + V\frac{\partial v}{\partial y} = 0. \tag{3b}$$

Here, u and v are the x and y components of the velocity field, and U and V are the x and y components of the pattern-translation vector. We can also think of (3a) and (3b) as $D_p u/Dt = 0$ and $D_p v/Dt = 0$, where $D_p/Dt \equiv \partial/\partial t + U\partial/\partial x + V\partial/\partial y$ is the rate of change following the pattern (i.e., not following an air parcel).

To motivate use of the frozen-turbulence constraint in time interpolation, consider a thought experiment in which the u field is identically zero and the v field is an eastward-translating ($U > 0$, $V = 0$) top-hat function (Fig. 1). Data are available at $t = 0$ and $t = \Delta t$, with the top hat centered on $x = x_0$ at the first data input time and on $x = x_0 + U\Delta t$ at the second data input time. If linear interpolation were used to analyze the v field at intermediate times ($0 < t < \Delta t$), the translating top-hat function would be misrepresented as two stationary top-hat functions: one that decays, and one that emerges and amplifies. In contrast, a frozen-turbulence-based procedure that analyses the v field at intermediate times in terms of v data at $t = 0$ that are advected forward in time with speed U, and/or v data at $t = \Delta t$ that are advected backward in time would correctly account for the translation of the single top-hat function across the time interval. This thought experiment also reveals potential differences between the motion of patterns and the motion of air parcels; here the pattern-translation paths are parallel to the x axis (since $V = 0$) while the parcel trajectories are parallel to the y axis (since $u = 0$).

Advection correction procedures have been used extensively in hydrology and in mesoscale and radar meteorology—for example, in accumulated rainfall estimation (Fabry et al. 1994; Ciach et al. 1997; Anagnostou and Krajewski 1999; Tabary 2007; Villarini and Krajewski 2010; Nielsen et al. 2014) and in multiple–Doppler radar wind and vertical velocity analysis (Carbone 1982; Chong et al. 1983; Roberts and Wilson 1995; Dowell and Bluestein 1997, 2002; Cifelli et al. 2002; Liu et al. 2004; Wurman et al. 2007; Marquis et al. 2008, 2012, 2014; Frame et al. 2009; Kosiba and Wurman 2014). However, the use of advection correction to reduce errors in the temporal interpolation step in trajectory calculations, as advocated in our study, is a relatively new application. Examples of such an application are the dual-Doppler analyses of Marquis et al. (2008, 2012) and Frame et al. (2009) and the EnKF trajectory analyses of Marquis et al. (2012, 2014), all of which used relatively simple translation-analysis formulations such as calculating trajectories in a storm-relative reference frame.

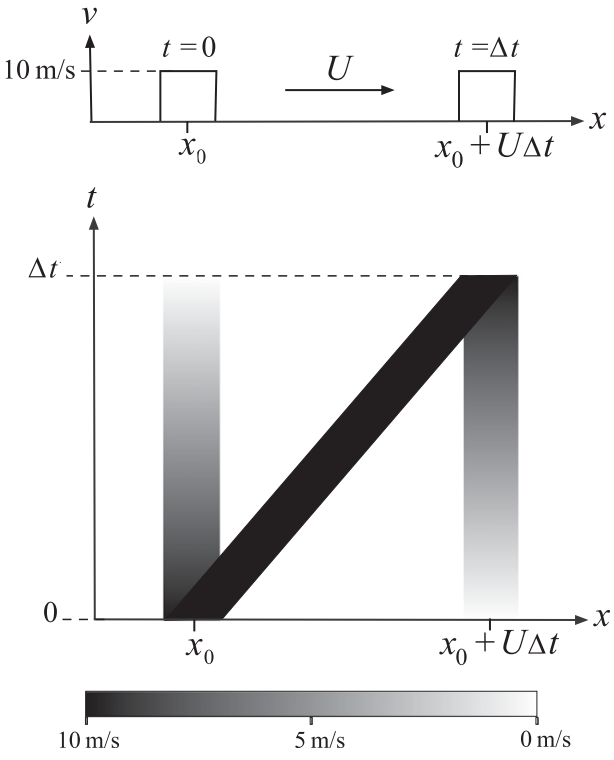

FIG. 1. Linear-in-time and advection-correction-based interpolations for a v field in the form of a top hat that translates in the x direction with speed U. The v field is shown (top) at two data input times $t = 0$ s and $t = \Delta t$ and (bottom) as a continuous function of time in the x–t plane, where it appears as a slanted solid black ribbon with slope $dx/dt = U$ (black represents peak value $v = 10\,\mathrm{m\,s^{-1}}$). The linear-in-time interpolated v field appears in the x–t plane as two stationary bands (slope $dx/dt = 0\,\mathrm{m\,s^{-1}}$), one decaying from 10 to $0\,\mathrm{m\,s^{-1}}$ and the other amplifying from 0 to $10\,\mathrm{m\,s^{-1}}$. An advection-correction-based interpolated v field using the correct translation speed U, whether it be via forward-in-time advection, backward-in-time advection, or a combined procedure, reproduces the true v field exactly since it translates in the same manner as the true v field.

The paper is arranged as follows. The technical details of the trajectory and advection correction procedures are provided in section 2. In section 3, analytical tests are used to verify that the numerical modules for these procedures are free of code errors. In section 4, the utility of the advection correction procedure is explored in tests with a high-resolution numerically simulated supercell storm dataset. A brief summary follows in section 5.

2. Methodology

a. *Nature of the experiments*

The purpose of our study is to demonstrate that replacing the standard linear time interpolation step in trajectory calculations with an advection correction procedure can

effectively reduce trajectory position errors, especially in cases where the input data are of coarse temporal resolution, and to understand the potential weaknesses and strengths of the approach. Tests are conducted using output from a high-resolution numerical storm simulation because that provides a convenient framework to explore the nature of the analysis errors. However, the advection-corrected trajectory procedure itself may find wider applications than in numerical convective storm modeling, for example, in trajectory analyses using multiple–Doppler radar–derived wind fields or in some of the other applications noted in the introduction.

We believe the goals of the study can be accomplished most efficiently in a two-dimensional framework, since trajectory and advection correction modules are then simpler to implement and verify (e.g., against analytical solutions), and run times with the high-resolution simulated storm dataset are shorter and less memory intensive. Given our limited computational resources, the two-dimensional framework allows us to conduct a much more extensive and systematic exploration of the analysis procedure, including the threat of solution nonuniqueness for the pattern-translation components. Moreover, if advection correction does not add value to trajectory analysis in the two-dimensional framework, there is little point in extending it to three dimensions.

We compute backward trajectories on an unstaggered horizontal (x, y) Cartesian analysis grid using low-altitude u and v (but not w) data. Experiments focus on the temporal resolution of the input data and on variations of implementing the advection correction. In each experiment, the trajectories are compared with a set of reference (verification) trajectories obtained using the linear time interpolation procedure with very-high-temporal-resolution input data from the numerical model. However, since w data are not used in any of our trajectory analyses, the reference trajectories may be quite different from the "true" trajectories. Even very low-altitude trajectories have been shown to be strongly dependent on the w field in these types of numerical experiments (Dahl et al. 2012). Further differences between reference and true trajectories likely follow from the interpolation of the numerical data on the model's staggered grid to the unstaggered analysis grid. Thus, while our current two-dimensional implementation provides a fair basis for comparing results from the linear time interpolation and advection correction procedures, the particular trajectories obtained in these tests should not be used to gain insights into convective-scale flow fields or dynamics.

In each experiment, we evaluate the position errors of air parcels launched backward in time from the analysis grid points at a common start time. The trajectories are determined by numerically integrating (1) using gridded u and v fields to estimate the parcel velocity at the instantaneous parcel location. The gridded u and v fields are obtained through one of two temporal interpolation procedures: standard linear interpolation (LI) or advection correction (AC). The basic AC procedure is described next.

b. Advection correction

The AC procedure removes the artificial stationary disappearance and emergence of analyzed features when linear time interpolation is used (as in Fig. 1) by accounting for the translation of features between successive data input times. The procedure is schematized in Fig. 2. Between two consecutive data input times is a succession of computational times.[2] At each computational time we consider an analysis grid on which each grid point serves as a home point for a pair of virtual "particles." From each home point, one particle is launched forward in time until the second data input time is reached, and the other particle is launched backward in time until the first data input time is reached. The particles translate with the pattern-translation components U and V estimated at the home point and time (estimation described in section 2c). More accurately, U and V are used in the forward translation, while $-U$ and $-V$ are used in the backward translation. The arrival locations of the particles at the data input times are noted and the u and v values at those locations are estimated via bilinear interpolation of u and v data from the neighboring grid points. The interpolated u and v values are then linearly interpolated (in a Lagrangian sense) to the home-point location and time.

c. Determining U and V

A variety of subjective and objective procedures have been used to estimate pattern-translation components in meteorological applications (Shapiro et al. 2010, their section 1). In the majority of the AC experiments in our present study, U and V are estimated using a two-dimensional version of a radar reflectivity-based procedure introduced by Gal-Chen (1982), with the u field used in place of reflectivity.[3] The Gal-Chen technique,

[2] The computational times are the same for the advection correction procedure and the subsequent Runge–Kutta integration used to calculate the trajectories.

[3] If the frozen-turbulence concept is appropriate for a given flow field then it should be applicable to the vector velocity field and to the individual Cartesian velocity components. This can be checked by comparing the U and V values obtained from the frozen-turbulence constraint applied to the u field, to the corresponding values obtained from the v field, and to the values obtained from a combination of u and v [as in Gal-Chen's (16)]. For the numerically simulated storm dataset considered in this study, the values of U and V obtained using the v field were very similar to those obtained using the u field.

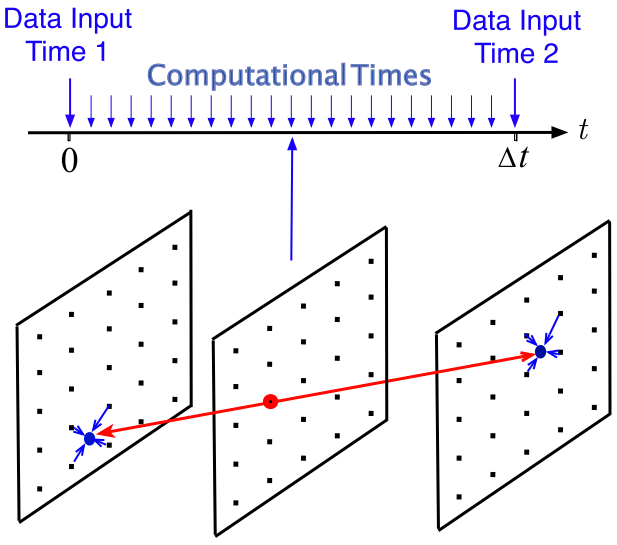

FIG. 2. Schematic of the advection correction procedure. At each computational time, each analysis grid point serves as a home point (red dot) for a pair of virtual particles. One particle is launched forward in time with pattern-translation components U and V until the second data input time is reached, and the other particle is launched backward in time with pattern-translation components $-U$ and $-V$ until the first data input time is reached. The red line connecting the home point to the two arrival locations and times marks the translation path. The u and v data at the data input times are bilinearly interpolated to the two particles' arrival locations (blue dots) from neighboring grid points (blue arrows around blue dots). These interpolated u and v values are then linearly interpolated to the home-point location and time.

which we now briefly summarize, is a simple example of a weak-constraint analysis (Sasaki 1970). A cost-function J that quantifies the squared error in the frozen-turbulence constraint (3a) is defined as

$$J(U,V) \equiv \iiint \left(\frac{\partial u}{\partial t} + U\frac{\partial u}{\partial x} + V\frac{\partial u}{\partial y}\right)^2 dx\,dy\,dt, \quad (4)$$

where the integration extends over the interval between two consecutive data input times and over a horizontal analysis domain. In this study, the integrations are performed over nonoverlapping subdomain boxes, partitions of the full analysis domain; U and V are considered constant over each subdomain box and over the time interval between the two data input times. To find U and V for which the error is a minimum, set $\partial J/\partial U = 0$ and $\partial J/\partial V = 0$, obtaining

$$AU + BV = D \quad \text{and} \quad (5a)$$
$$BU + CV = E, \quad (5b)$$

where

$$A \equiv \iiint \left(\frac{\partial u}{\partial x}\right)^2 dx\,dy\,dt, \quad B \equiv \iiint \frac{\partial u}{\partial x}\frac{\partial u}{\partial y}dx\,dy\,dt,$$
$$C \equiv \iiint \left(\frac{\partial u}{\partial y}\right)^2 dx\,dy\,dt, \quad D \equiv -\iiint \frac{\partial u}{\partial t}\frac{\partial u}{\partial x}dx\,dy\,dt, \quad \text{and}$$
$$E \equiv -\iiint \frac{\partial u}{\partial t}\frac{\partial u}{\partial y}dx\,dy\,dt. \quad (6)$$

In our study, the time derivatives in (6) are approximated by centered finite-difference expressions with a time step consistent with the Runge–Kutta computational time step. Equations (5a) and (5b) are solved for U and V as

$$U = \frac{CD - EB}{AC - B^2} \quad \text{and} \quad V = \frac{AE - BD}{AC - B^2}. \quad (7)$$

To confirm that this solution corresponds to a minimum instead of a maximum, we define

$$Q \equiv \frac{\partial^2 J}{\partial U^2}\frac{\partial^2 J}{\partial V^2} - \left(\frac{\partial^2 J}{\partial U \partial V}\right)^2, \quad (8)$$

where

$$\frac{\partial^2 J}{\partial U^2} = 2\iiint \left(\frac{\partial u}{\partial x}\right)^2 dx\,dy\,dt,$$
$$\frac{\partial^2 J}{\partial V^2} = 2\iiint \left(\frac{\partial u}{\partial y}\right)^2 dx\,dy\,dt, \quad \text{and}$$
$$\frac{\partial^2 J}{\partial U \partial V} = 2\iiint \frac{\partial u}{\partial x}\frac{\partial u}{\partial y}dx\,dy\,dt. \quad (9)$$

Since $\partial^2 J/\partial U^2$ is clearly positive, while Schwarz's inequality for integrals applied to the last term in (8) reveals that Q is also positive, the second-derivative rule for distinguishing maxima and minima (Courant 1988, p. 207) establishes that the solution is a minimum.

A word of caution is in order, however, in cases where gradients in the u field (or whatever variable is being tracked) are small over an entire subdomain box. In such cases the expressions in (7) become very sensitive to small changes in the u field, and the problem becomes ill posed.[4] Essentially, the Gal-Chen procedure—and many other pattern-tracking algorithms—break down when there is no pattern to track.

Following Gal-Chen's (1982) recommendation, we implement an iterative version of this procedure. Since U and V are not known prior to the first evaluation of the integrals

[4] Theoretically, if u is constant over a subdomain box then all of the integrals in (6) vanish and (7) becomes indeterminate. In this case J is identically zero for any pair of U and V values.

in (6), first guesses for U and V are required to start the procedure. Using these first-guess values, u and v at every home point at every computational time is advection corrected following the procedure of section 2b. The advection-corrected u and v fields are then used to evaluate the integrals in (6), which are then used in (7) to update U and V. The procedure then iterates, with each cycle consisting of an advection correction for u and v, an evaluation of (6), and an evaluation of (7). The procedure is terminated after 20 iterations (although, in practice, the procedure often converges after just a few iterations), at which point the changes in U and V from the nineteenth iteration are noted. If the magnitudes of the changes in U and V are each less than a threshold value ($0.1\,\mathrm{m\,s^{-1}}$), the procedure is deemed to have converged, and the final advection-corrected u and v fields are used in the trajectory calculation. The incidences of nonconvergence are monitored. Although the iterative procedure is applied separately to each subdomain box, the virtual particles launched from each of the home points within a subdomain box are free to leave the box; their arrival locations at the data input times, whether within the box or external to it, are noted and the subsequent interpolations proceed as in section 2b.

In a converged iterative solution, the integrals in (6) are, implicitly, functions of U and V, the "linear" algebraic equations in (5a) and (5b) are actually nonlinear, and solution uniqueness for U and V cannot be guaranteed. Indeed, as shown in Shapiro et al. (2010, their section 5), a wide class of advection correction/analysis procedures, including the Gal-Chen procedure, is potentially subject to nonuniqueness associated with temporal aliasing. Mindful of this threat, we ran advection correction experiments with different first-guess assignments for U and V, and in some cases explicitly used (4) to evaluate $J(U, V)$ for a large range of U and V.

d. Trajectory calculations

The air parcel trajectories $\mathbf{x}(t, \mathbf{x}_0)$ are obtained by integrating (1) using a fourth-order Runge–Kutta scheme (Chapra and Canale 2005). The parcels are initially far enough from the model's lateral boundaries that in no experiment do any of them leave the model domain over the 5-min backward-integration period. Bilinear spatial interpolation is used to estimate u and v at the instantaneous parcel location from gridded u and v fields at the vertices of the grid box enclosing the parcel. These gridded u and v fields were obtained through AC estimations (described in sections 2b and 2c) or LI estimations, all at the same computational times used in the Runge–Kutta integrations.

e. Error statistics

Trajectory errors are quantified after 5 min of backward integration. The individual displacement error (IDE) quantifies the distance between the end point of a trajectory in an AC or LI experiment and the end point of the corresponding reference trajectory:

$$\mathrm{IDE}^i_{\mathrm{EXP}} \equiv \sqrt{(x^i_{\mathrm{EXP}} - x^i_R)^2 + (y^i_{\mathrm{EXP}} - y^i_R)^2}. \quad (10)$$

Here, the subscript EXP denotes the experiment type (AC or LI), x^i_{EXP} and y^i_{EXP} are the end-point coordinates of the ith trajectory in the experiment, and x^i_R and y^i_R are the end-point coordinates of the ith reference trajectory.

The difference in the end-point location errors between an AC experiment and the corresponding LI experiment are quantified by a differenced individual displacement error (ΔIDE),

$$\Delta\mathrm{IDE}^i \equiv \mathrm{IDE}^i_{\mathrm{LI}} - \mathrm{IDE}^i_{\mathrm{AC}}. \quad (11)$$

A positive (negative) value of $\Delta\mathrm{IDE}^i$ indicates that a trajectory in an AC experiment is closer to (further from) the reference trajectory than is the trajectory in the corresponding LI experiment.

The mean displacement error (MDE) and differenced mean displacement error (ΔMDE) are computed as averages of the above statistics over a population of N trajectories:

$$\mathrm{MDE}_{\mathrm{EXP}} \equiv \frac{1}{N}\sum_{i=1}^{N} \mathrm{IDE}^i_{\mathrm{EXP}} \quad \text{and} \quad (12)$$

$$\Delta\mathrm{MDE} \equiv \mathrm{MDE}_{\mathrm{LI}} - \mathrm{MDE}_{\mathrm{AC}}, \quad (13)$$

where the subscript EXP is, again, a placeholder for AC or LI. The MDE, also known as the mean absolute horizontal transport deviation (AHTD) or error, is commonly used to quantify errors in trajectory analyses (Kuo et al. 1985; Rolph and Draxler 1990; Doty and Perkey 1993; Stohl et al. 1995, 2001; Stohl 1998; Harris et al. 2005; Riddle et al. 2006; Miltenberger et al. 2013).

3. Analytical verification tests

Tests with a two-dimensional (x, y) analytical wind field that satisfied the frozen-turbulence constraints in (3a) and (3b) exactly were conducted to verify that there were no errors in the numerical codes for the Runge–Kutta integration, bilinear spatial interpolation, linear time interpolation, or advection correction procedures. It is well known that in two-dimensional incompressible flows, u and v can be written in terms of a streamfunction ψ by $u = \partial\psi/\partial y, v = -\partial\psi/\partial x$ (Kundu 1990) and that streamlines and trajectories coincide if the flow is in a steady state (in which case ψ is a conserved scalar). The analytical wind field is not in a steady state but, as we will see, its satisfaction of the frozen-turbulence constraint allows us to

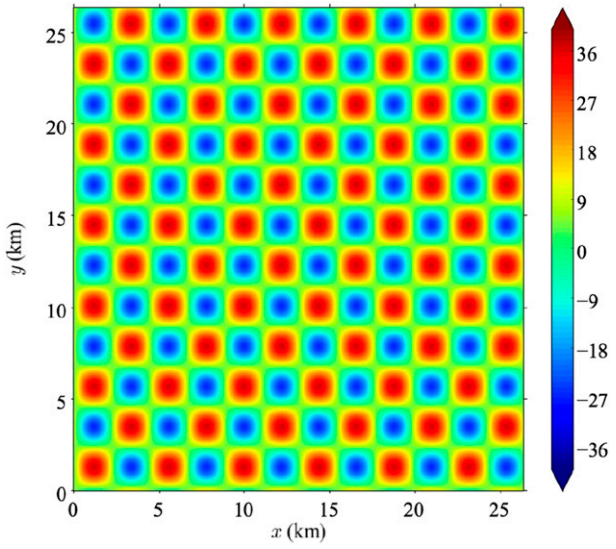

FIG. 3. The u field (m s^{-1}) in the analytical verification tests.

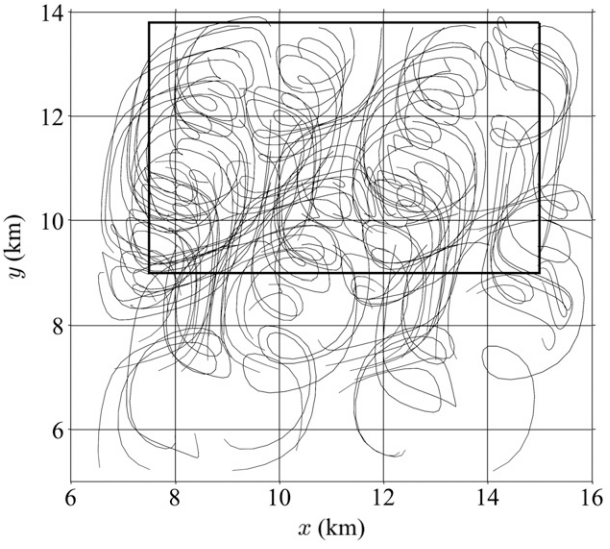

FIG. 4. Zoomed-in view of sample trajectories from 5 min of backward integration. The trajectories originated in a subdomain extending approximately from $x = 7.5$ to 15 km and from $y = 9$ to 14 km, and tended to migrate (backward in time) toward the southwest. Trajectories are shown only for parcels launched every fifteenth grid point (in x and y).

derive a conservation principle for a perturbation streamfunction ψ' that can be used in verification tests.

Let $f(x, y)$ represent the streamfunction for any steady two-dimensional disturbance that satisfies the equations of motion (e.g., the Euler equations). Then the en masse transport of that disturbance by a uniform current with components U and V is described by the streamfunction,

$$\psi = Uy - Vx + \psi', \tag{14}$$

where $\psi' = f(\xi, \eta)$, $\xi \equiv x - Ut$, and $\eta \equiv y - Vt$. Now consider the material derivative D/Dt ($\equiv \partial/\partial t + u\partial/\partial x + v\partial/\partial y$) of ψ'. From the chain rule and the relations $\partial\xi/\partial x = 1$, $\partial\xi/\partial t = -U$, $\partial\eta/\partial y = 1$, $\partial\eta/\partial t = -V$, $u = \partial\psi/\partial y = U + \partial f/\partial\eta$, and $v = -\partial\psi/\partial x = V - \partial f/\partial\xi$, we find that

$$\begin{aligned}\frac{D\psi'}{Dt} &= \frac{\partial f}{\partial\xi}\frac{\partial\xi}{\partial t} + \frac{\partial f}{\partial\eta}\frac{\partial\eta}{\partial t} + u\frac{\partial f}{\partial\xi}\frac{\partial\xi}{\partial x} + v\frac{\partial f}{\partial\eta}\frac{\partial\eta}{\partial y} = -U\frac{\partial f}{\partial\xi} - V\frac{\partial f}{\partial\eta} + u\frac{\partial f}{\partial\xi} + v\frac{\partial f}{\partial\eta} \\ &= -U\frac{\partial f}{\partial\xi} - V\frac{\partial f}{\partial\eta} + \left(U + \frac{\partial f}{\partial\eta}\right)\frac{\partial f}{\partial\xi} + \left(V - \frac{\partial f}{\partial\xi}\right)\frac{\partial f}{\partial\eta} = \frac{\partial f}{\partial\eta}\frac{\partial f}{\partial\xi} - \frac{\partial f}{\partial\xi}\frac{\partial f}{\partial\eta} = 0;\end{aligned} \tag{15}$$

that is, ψ' is conserved following air parcel motion.

The analytical tests are based on a translating inviscid version of Taylor's vortex grid (Rosenhead 1963, p. 139). With the perturbation streamfunction considered in the form

$$\psi' = A\cos\left(\pi\frac{x - Ut}{d}\right)\cos\left(\pi\frac{y - Vt}{d}\right), \tag{16}$$

the corresponding wind components are

$$u = U - \frac{A\pi}{d}\cos\left(\pi\frac{x - Ut}{d}\right)\sin\left(\pi\frac{y - Vt}{d}\right) \quad \text{and} \tag{17a}$$

$$v = V + \frac{A\pi}{d}\sin\left(\pi\frac{x - Ut}{d}\right)\cos\left(\pi\frac{y - Vt}{d}\right). \tag{17b}$$

We evaluate (17a) and (17b) on a 26.4 km × 26.4 km Cartesian grid with a grid spacing of $\Delta x = \Delta y = 30$ m and parameter values of $A = 7000\pi$ m^2 s^{-1}, $d = 700\pi$ m, $U = 5$ m s^{-1}, and $V = 10$ m s^{-1}. The u field at the time the trajectories were launched is shown in Fig. 3.

Tests were conducted with 40 411 backward trajectories launched from all grid points within an analysis subdomain (rectangle) extending approximately from $x = 7.5$ to $x = 15$ km and from $y = 9$ to $y = 14$ km. The trajectories were integrated backward in time for 5 min using a computational time step of 0.1 s. The reference trajectories were computed with the LI procedure applied to input data of high temporal resolution ($\Delta t = 1$ s). Sample reference trajectories over the course of the backward integration are shown in Fig. 4. Despite the

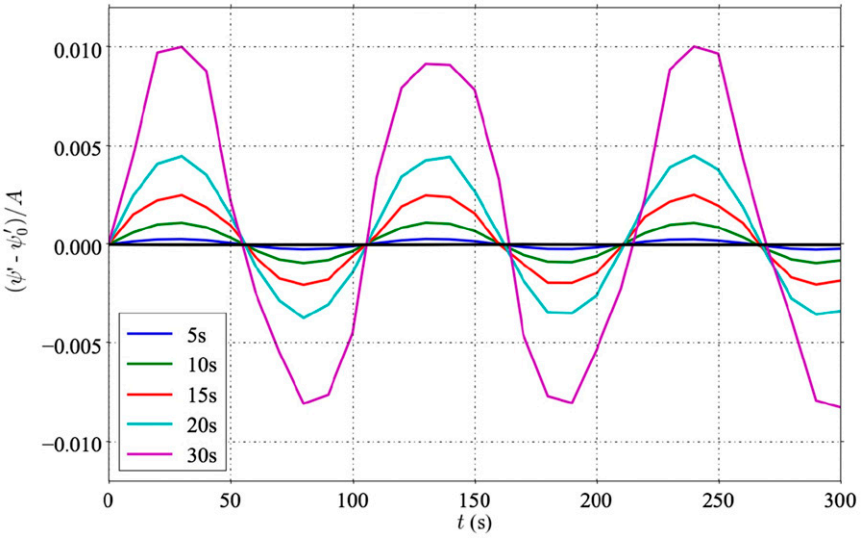

FIG. 5. Nondimensional deviation of a selected air parcel's perturbation streamfunction ψ' from its initial value ψ'_0 in LI and AC experiments (the latter run with subdomain boxes of 3.3-km width) over 5 min of backward integration for the data input time intervals indicated in the legend. The nondimensional deviations in the reference run (LI using $\Delta t = 1$ s) and in the AC experiments for all data input time intervals are so close to zero that the individual curves lie on top of each other (solid black curve). Results from the LI experiments with the larger data input time intervals get progressively worse as the data input time interval increases.

smooth appearance of the flow field, the trajectories appear rather chaotic.

The LI and AC experiments were run using data input time intervals Δt = 1, 5, 10, 15, 20, and 30 s (LI using $\Delta t = 1$ s was the reference experiment). The AC experiments were run with U–V pairs computed on nonoverlapping subdomain boxes of widths 1.2, 2.4, 3.3, and 4.38 km. On each subdomain box, a U–V pair was determined from 20 iterations of the Gal-Chen procedure initialized with first-guess values for U and V of 0 m s^{-1}.

For all data input time intervals and box sizes, the retrieved U and V values converged rapidly (three or four iterations) to the correct values. At the end of 20 iterations, the errors in U and V remained on the order of 0.01 m s^{-1}. With the retrieved values used in the AC experiments, the deviation of an air parcel's perturbation streamfunction ψ' from its initial value ψ'_0 was typically less than a fraction of 0.1% of the perturbation streamfunction amplitude A. In the LI reference run ($\Delta t = 1$ s), the deviations were also typically less than a fraction of 0.1% of A, but the deviations in the other LI experiments increased rapidly with Δt. The nondimensional deviations for a representative trajectory are shown in Fig. 5.

In the AC experiments, the $\mathrm{MDE_{AC}}$ were very small; they ranged from about 1 m in the Δt = 1-s experiments to about 4 m in the Δt = 30-s experiments and were insensitive to box size. In contrast, in the LI experiments, $\mathrm{MDE_{LI}}$ increased from about 10 m in the Δt = 5-s experiment to about 320 m in the Δt = 30-s experiment.

The near-zero values of the nondimensional deviation ψ' in all of the AC experiments and in the LI reference run, along with the very small values of $\mathrm{MDE_{AC}}$, suggest that our trajectory analysis codes are free of errors. However, since the wind field satisfies the frozen-turbulence constraint exactly, the analytical test cannot provide insight into how well the AC procedure might work under more realistic meteorological conditions—for example, where different wind-field features propagate with different speeds, or where wind-field features amplify or decay.

4. Tests with a 30-m simulation of a supercell storm

a. *Description of the dataset*

Low-altitude wind data were sampled from the inner grid of a high-resolution numerically simulated tornadic-supercell-storm dataset described in a previous study (Orf et al. 2014). These data were generated using a three-dimensional nonhydrostatic cloud model, version 16 of Cloud Model 1 (CM1; Bryan and Morrison 2012). Nested within an outer grid of size 120 km × 120 km × 20 km, the inner grid covers a 60 km × 60 km × 10 km domain with a 30-m isotropic grid spacing. The model was run with a Morrison two-moment cloud microphysics parameterization and a Smagorinsky turbulence closure. The lower

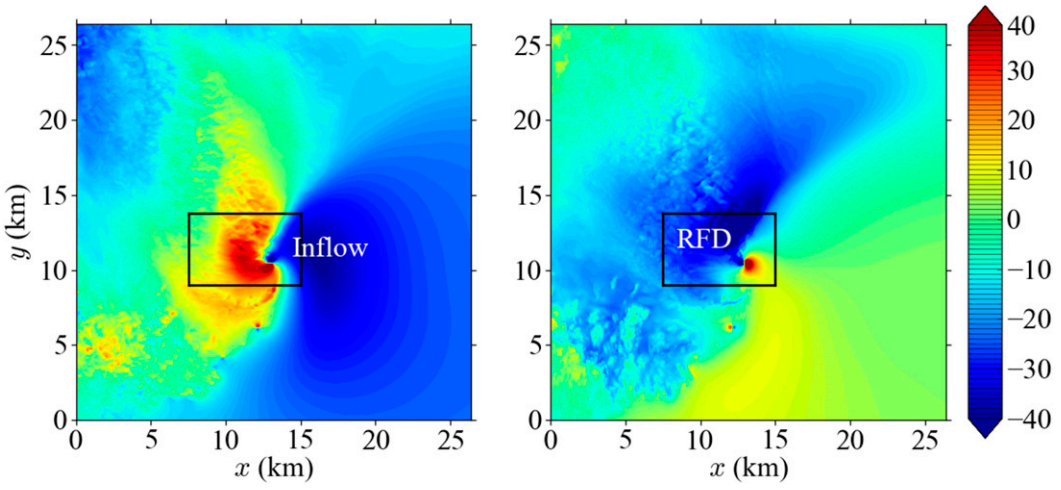

FIG. 6. Cross section of (left) u and (right) v (both in m s^{-1}) sampled from the z = 45-m level of the simulated supercell dataset at model time t = 6610 s. Backward trajectories are launched from all grid points within the inset rectangle. The rectangle includes strong easterly winds ($u < 0$) associated with the storm inflow and strong northerly winds ($v < 0$) associated with the RFD.

boundary was free slip. Convection was initiated using an updraft nudging technique in a horizontally homogeneous environment specified by a 1-h RUC forecast sounding located off the right flank of the 24 May 2011 Calumet–El Reno–Piedmont–Guthrie supercell storm. It is important to note that the model was integrated in a moving reference frame designed to keep the storm relatively stationary near the center of the model domain.

In preparation for the trajectory experiments, 5 min of storm-relative u and v data on the model's C grid (from model times 6310 to 6610 s) were extracted from the z = 45-m level at 1-s intervals and interpolated to an unstaggered trajectory analysis grid with 30-m grid spacing. The wind fields at the start time of the backward integrations (t = 6610 s) are shown in Fig. 6. At this time the storm is in a mature phase, with a wind couplet suggestive of a large tornado[5] centered at $x \approx 13$ km, $y \approx 10$ km, strong northerly rear-flank downdraft (RFD) winds west of the tornado, and a region of strong storm-relative inflow extending east of the tornado. There are notable differences in the amplitudes of the small-scale features in the RFD and inflow regions. The wind fields in the inflow region appear smooth and laminar, while the wind fields in the RFD are ragged and streaked with small-scale roll-like or wavy structures. Animations of the u and v data (not shown) suggest that these small-scale features tend to move with the prevailing northerly winds. In contrast, the wind fields in the inflow region, which tend to lack small-scale features, appear nearly stationary, indicating that the wind pattern propagates with the storm. These differences have an important bearing on the advection correction results.

b. Experiments and results

Since the model storm was relatively stationary (by design), a pair of U–V values close to zero would correctly characterize the storm motion, and an advection correction procedure that used such small values over the whole domain would behave like a linear time interpolation procedure. Accordingly, against the backdrop of near-zero

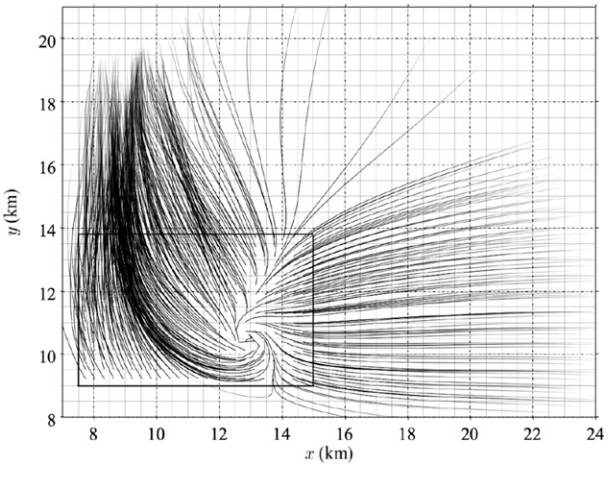

FIG. 7. Selected 5-min backward reference trajectories. Trajectories are launched from within the inset rectangle at model time t = 6610 s.

[5] This long-lived vortex persisted throughout the 5-min analysis time window with peak winds (>100 m s^{-1}) exceeding the limits of the color bar scale. A smaller, weaker, and shorter-lived vortex is apparent approximately 4 km south of the primary vortex.

TABLE 1. Summary of experiments. Experiments were run using data of progressively coarser time resolution: $\Delta t = 5$, 10, 15, 20, and 30 s. AC experiments were run with U and V calculated on subdomain boxes of widths 1.2, 2.4, 3.3, and 4.38 km.

Name	Description
LI	Linear time interpolation.
AC-GC1	Iterative Gal-Chen-based advection correction procedure initialized with one first-guess U–V pair per box, the box-averaged u and v.
AC-GC9	Iterative Gal-Chen-based advection correction procedure seeded with nine first-guess U–V pairs per box, the nine permutations of 0, 20, and $-20\,\mathrm{m\,s^{-1}}$, taken two at a time. The smallest J defined the U, V used in the advection correction.
AC-MW	Advection correction based on the mean wind: U and V were set equal to the box-averaged u and v (no first guesses needed in this direct procedure).

storm motion, we viewed the use of local estimation procedures for U and V as essential if we were to show how advection correction could add value to trajectory analyses. In this study, local estimates of U–V pairs were computed on subdomain boxes, as in the verification tests. Use of U and V fields obtained from the continuous spatially variable procedure of Shapiro et al. (2010) will be tested in a future study.

In each experiment, 40 411 backward trajectories were launched from all grid points within the rectangle shown in Fig. 6. The trajectories were integrated backward for 5 min using a computational time step of 0.1 s. The reference trajectories were generated from the LI procedure as applied to the 1-s input data. Trajectories computed using AC procedures with the same input data yielded nearly identical results (not shown). The sample reference trajectories shown in Fig. 7 reveal convergent flow structures (in a forward-in-time sense), which pose a challenging divergent flow scenario for accurate backward trajectory analysis (Dahl et al. 2012; Schenkman 2012, chapter 5).

In this section, results from several variants of the AC procedure are compared to results from the LI procedure. The variant types (described below) are summarized in Table 1. All LI and AC experiments were conducted using data at time intervals Δt of 5, 10, 15, 20, and 30 s. In the AC experiments, U–V pairs were calculated on subdomain boxes of widths 1.2, 2.4, 3.3, and 4.38 km at every time interval throughout the integration period.

The individual displacement errors in the LI experiments, $\mathrm{IDE}^i_{\mathrm{LI}}$, are shown in Fig. 8. The $\mathrm{IDE}^i_{\mathrm{LI}}$ increased rapidly with Δt and, in the $\Delta t = 30$-s experiment, exceeded the 500-m limits on the grayscale bar in isolated swaths of the RFD, in the tornado, and along the gust front extending north and south of the tornado. Particularly large errors (on the order of several kilometers) were found in an elongated band along the gust front.

Two different first-guess options were tested for the iterative Gal-Chen procedure: experiments AC-GC1 and AC-GC9. In both experiments, convergence of the procedure was checked after 20 iterations, and U and V were set to zero in cases of nonconvergence.[6] In AC-GC1, the first guesses for U and V were specified on each subdomain box as the box-averaged values of u and v. As seen in Table 2, the incidences of nonconvergence in AC-GC1 were relatively infrequent, generally affecting just a few percent of the U–V pair estimates. However, there were trends for the incidences to increase with box size and data input time interval.

In experiments AC-GC9, the Gal-Chen procedure was run on each subdomain box with nine first guesses for U and V, the permutations of 0, 20, and $-20\,\mathrm{m\,s^{-1}}$ taken two at a time. For each first-guess pair, the converged U and V values and the advection-corrected u and v fields were used to evaluate J from (4). The advection-corrected winds corresponding to the smallest J were then used in the trajectory analysis. Incidences of nonconvergence for all nine first guesses were very rare (typically much less than 1% of possible occurrences).

We also conducted an advection correction experiment AC-MW [mean wind (MW)] in which U and V were specified on each subdomain box as the box-averaged values of u and v. In other words, the first-guess values in AC-GC1 were used to define U and V directly, in a noniterative, non-Gal-Chen procedure.

The MDEs from all experiments are shown in Fig. 9. The MDEs in the two Gal-Chen-based AC experiments, AC-GC1 and AC-GC9, were significantly less than in the corresponding LI experiments (typically 30%–50% less) for all Δt and box sizes. Of these two procedures, AC-GC1 outperformed AC-GC9 by about 10 m for the data input time intervals $\Delta t = 5$, 10, 15, and 20 s, but outperformed AC-GC9 by as much as 50 m for the

[6] Included in our tally of nonconverged U–V pairs were cases where U or V actually did converge—but to unrealistically large values ($>40\,\mathrm{m\,s^{-1}}$). Such cases were extremely rare, but when they occurred, we again set U and V to zero.

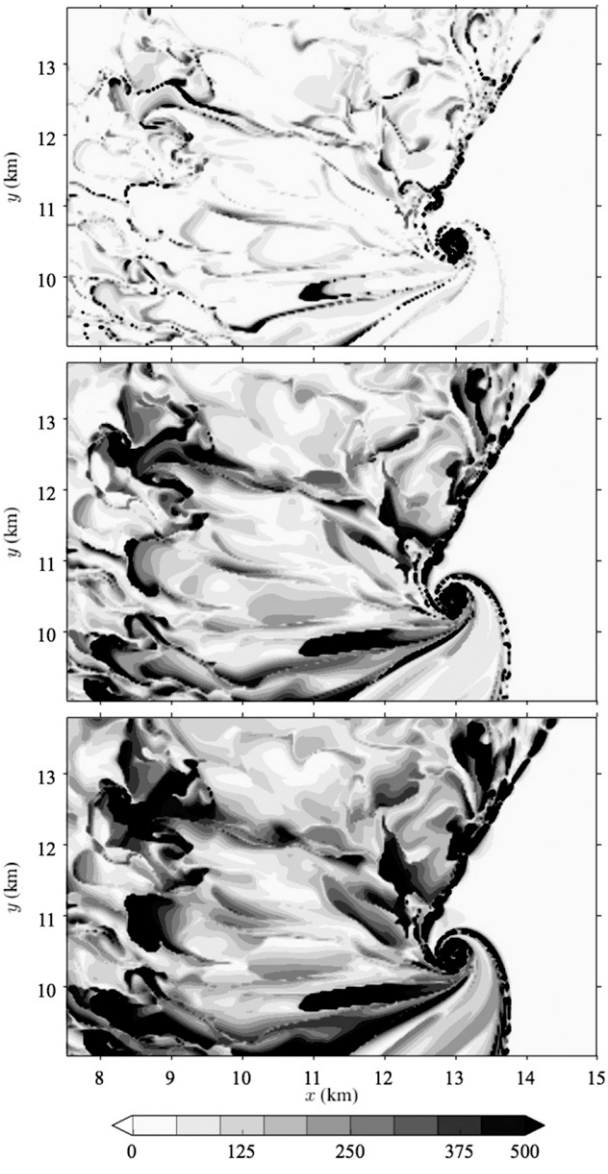

FIG. 8. Individual displacement errors IDE^i_{LI} (m) after 5 min of backward integration in LI experiments with data input time intervals of (top) 5, (middle) 15, and (bottom) 30 s. The error associated with each trajectory is plotted at the starting point of that trajectory (i.e., parcel location at $t = 6610$ s).

longest time interval, $\Delta t = 30$ s. The MDEs in the mean-wind-based AC experiments (AC-MW) were comparable to the MDEs in AC-GC1 and AC-GC9 for the two smaller box sizes but were notably larger than in AC-GC1 and AC-GC9 for the two larger box sizes. Indeed, the MDEs in the AC-MW experiment with the largest Δt and box width ($\Delta t = 30$ s, 4.38 km) actually exceeded the MDEs in the corresponding LI experiment.

Figure 9 also shows that the MDE improvements of the two Gal-Chen-based AC experiments over the LI

TABLE 2. Incidences of nonconvergence of the iterative Gal-Chen procedure in AC-GC1 experiments run with different subdomain box sizes and data input time intervals. The incidences are reported as the number of times the procedure failed to converge divided by the number of times the procedure was run (number of boxes times the number of data input intervals in the 5-min window) and are expressed as a percentage.

Box size (km)	Data input time interval (s)				
	5	10	15	20	30
1.2	1.2	1.1	1.6	3.3	8.8
2.4	1.3	1.4	2.7	3.9	10.1
3.3	2.8	2.8	3.2	5.4	8.6
4.38	6.3	6.3	6.6	7.1	14.4

experiments are on the order of 100 m. While these improvements appear to be small in an absolute sense, inspection of analysis-domain plots of ΔIDE^i puts these improvements in perspective. Consider the representative plots of ΔIDE^i shown in Fig. 10 for AC-GC1 run using $\Delta t = 5$, 15, and 30 s and a box width of 1.2 km. While the AC-GC1 errors were only slightly less than the LI errors in large regions of the analysis domain (cf. Fig. 10 to Fig. 8), the IDE^i_{LI} in many of those regions were small to begin with, so there was not much room for improvement. However, in several regions where the IDE^i_{LI} were large, for example, in isolated bands in the RFD and along the gust front, particularly north of the

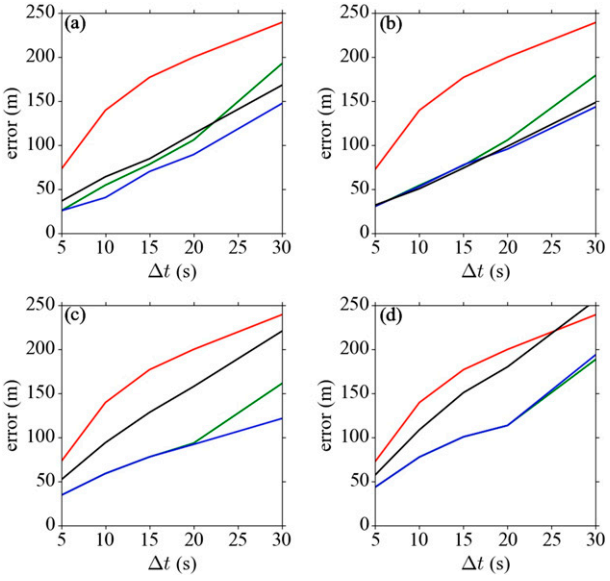

FIG. 9. MDEs vs data input time interval for the LI and AC experiments. In the AC experiments, U and V are computed on subdomain boxes of width (a) 1.2, (b) 2.4, (c) 3.3, and (d) 4.38 km. Errors are shown for LI (red curve), AC-GC9 (green curve), AC-GC1 (blue curve), and AC-MW (black curve).

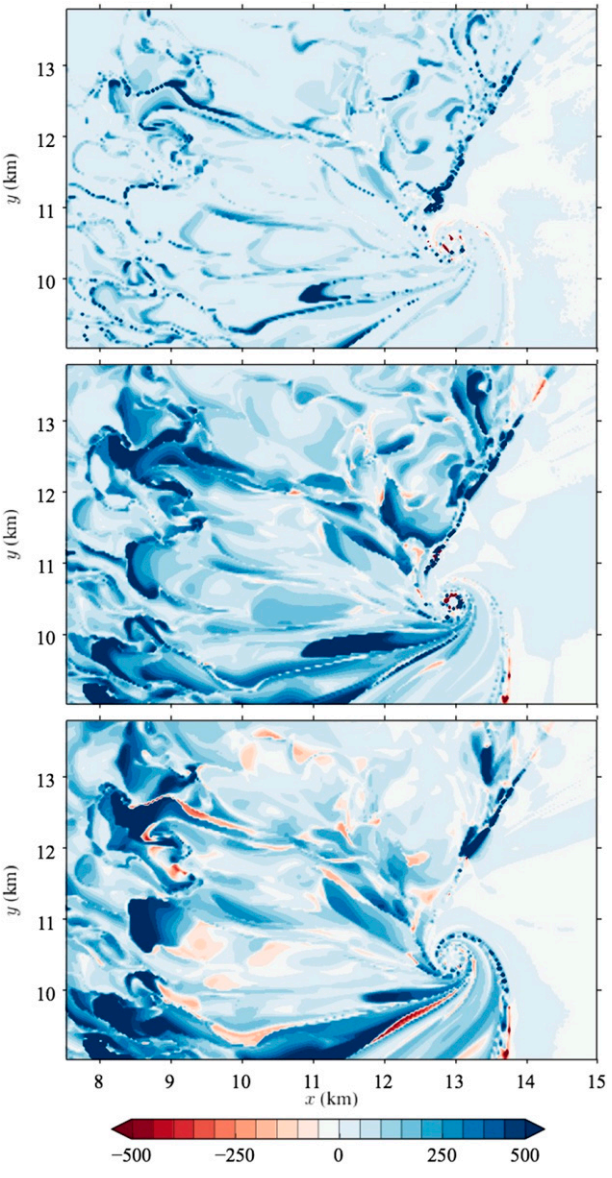

FIG. 10. Differenced individual displacement errors ΔIDE^i ($m\,s^{-1}$) in experiments AC-GC1 with U and V calculated on 1.2-km-wide subdomain boxes with Δt = (top) 5, (middle) 15, and (bottom) 30 s. The error associated with each trajectory is plotted at the starting point of that trajectory (i.e., parcel location at t = 6610 s). Blue (red) shading indicates regions where errors in an AC-GC1 experiment are less than (greater than) in the corresponding LI experiment. The IDE^i_{LI} field used in the construction of this plot is shown in Fig. 8.

tornado, the error reductions were substantial (>500 m). The representative histogram of ΔIDE^i shown in Fig. 11 (AC-GC1 run with Δt = 15 s and 1.2-km box widths) shows that (i) a large majority of trajectories are improved by the Gal-Chen-based AC procedure, (ii) most of the improvements are small in an absolute sense, but that (iii) there are thousands of points where the

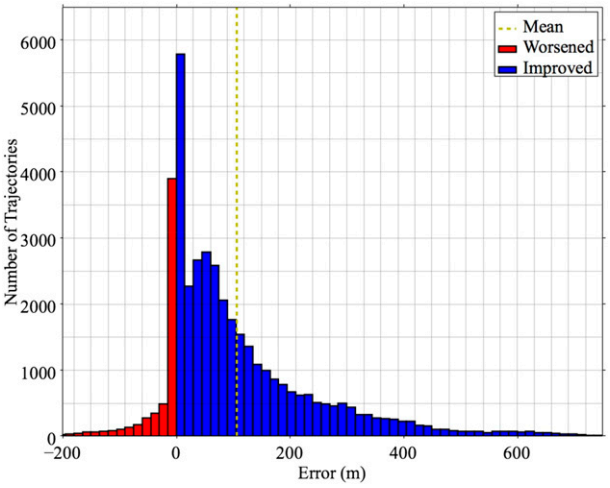

FIG. 11. Histogram of ΔIDE^i from experiment AC-GC1 run with U and V calculated on 1.2-km-wide subdomain boxes using data at time intervals of Δt = 15 s.

improvements exceed 200 m and hundreds of points where the improvements exceed 500 m.

The ΔIDE^i for the mean wind experiment AC-MW using Δt = 30 s and box widths of 1.2 km is shown Fig. 12. The results are striking: AC-MW performed well throughout the entire region west of the gust front, even outperforming AC-GC1 in that region (cf. Fig. 12 with bottom panel of Fig. 10) but performed poorly in the inflow region, especially in the vicinity of the gust front.

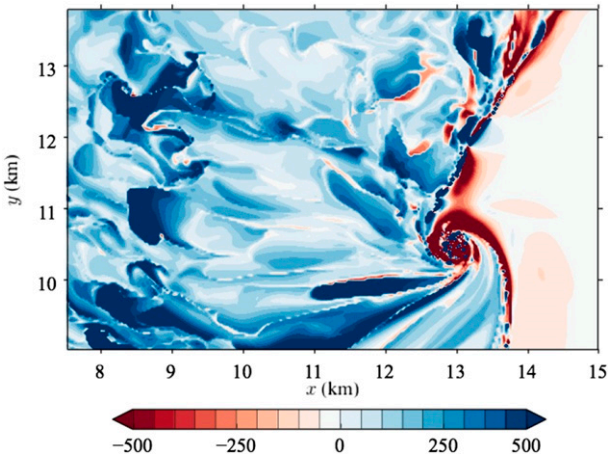

FIG. 12. Differenced individual displacement errors ΔIDE^i ($m\,s^{-1}$) in experiment AC-MW with U and V calculated as averages of u and v, respectively, on 1.2-km-wide subdomain boxes using data at time intervals of Δt = 30 s. The error associated with each trajectory is plotted at the starting point of that trajectory (i.e., parcel location at t = 6610 s). Blue (red) shading indicates regions where errors in AC-MW are less than (greater than) in the corresponding LI experiment. The IDE^i_{LI} field used in the construction of this plot is shown in Fig. 8.

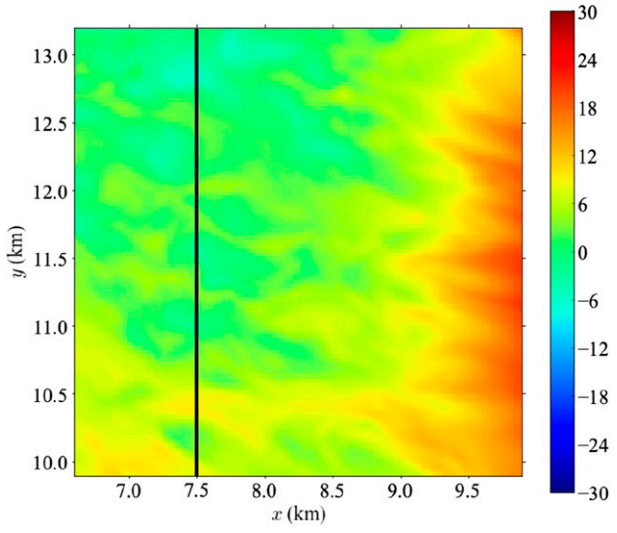

FIG. 13. Closeup view of the u field ($\mathrm{m\,s^{-1}}$) in a 3.3-km-wide subdomain box in the RFD at model time $t = 6550$ s. Solid line at $x = 7.5$ km marks western edge of the rectangle in Fig. 6.

c. Discussion

The two Gal-Chen-based AC experiments yielded results that were broadly superior to those obtained with linear time interpolation. Results from the Gal-Chen-based AC experiments also compared favorably to those from the mean-wind-based AC experiment. Between the two Gal-Chen-based experiments, use of a single first-guess U–V pair based on the mean-wind components (AC-GC1) outperformed use of multiple first guesses (AC-GC9). The fact that use of the mean wind for the first guess was desirable, but use of the mean wind for direct specification of the actual U and V was undesirable is somewhat paradoxical. We shed light on these and other results by examining the winds and cost function $J(U, V)$ in the RFD and inflow regions.

A closeup view of the u field in a 3.3-km-wide subdomain box in the RFD (Fig. 13) shows that the characteristic wavelengths of the previously noted small-scale roll/wavy disturbances are $\lambda \sim 500$ m. Applying the nonuniqueness analysis of Shapiro et al. (2010, their section 5) for a single wave to the present case (with V in place of U) suggests that U and V could be retrieved as

$$U \sim U_{\text{true}} \quad \text{and} \quad V \sim V_{\text{true}} + m\frac{\lambda}{\Delta t}, \tag{18}$$

where U_{true} and V_{true} are the actual pattern-translation components and $m\lambda/\Delta t$ is the mth aliased contribution (m is an integer). Animations of u in this RFD

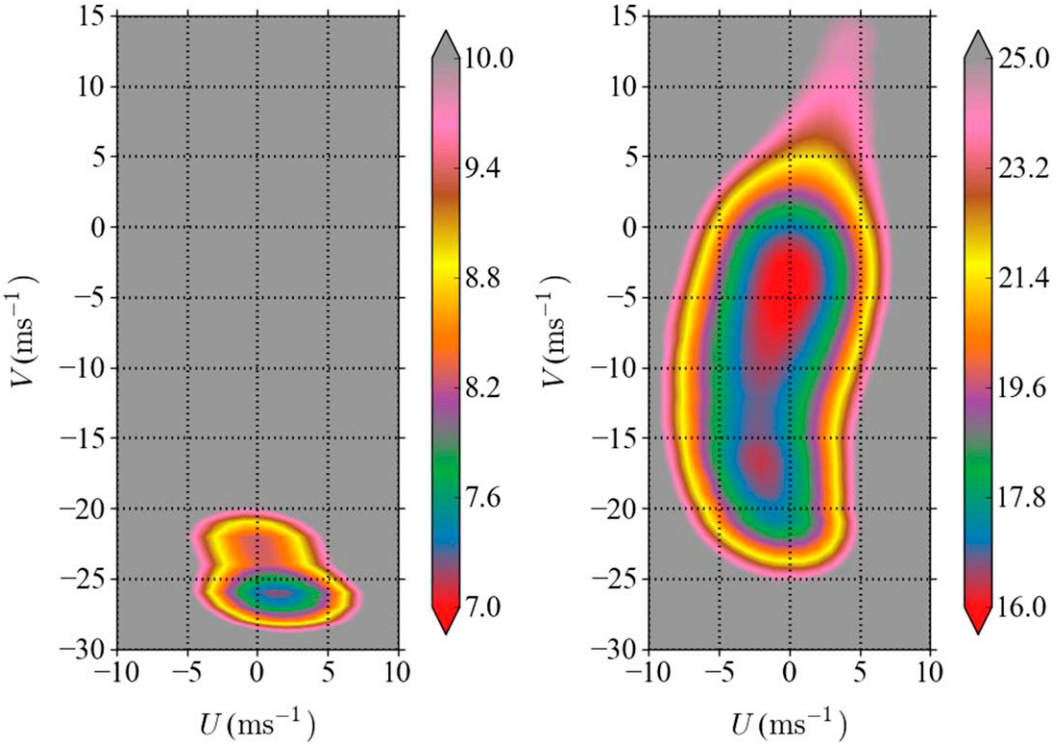

FIG. 14. Contour plot of $J(U, V)$ ($\mathrm{m^4\,s^{-3}} \times 10^3$) obtained by evaluating (4) for a range of specified U and V values. The analysis subdomain used in the evaluations of (4) is a 3.3-km-wide box located in the RFD (same box as in Fig. 13). Results are shown using data at time intervals (left) 5 and (right) 30 s. Data were used at times $t = 6650$ s and either $t = 6555$ s ($\Delta t = 5$ s) or $t = 6580$ s ($\Delta t = 30$ s).

subdomain show that the wavy disturbances translate with the prevailing northerly winds—that is, with V_{true} ranging from -20 to $-25\,\text{m s}^{-1}$, and $U_{\text{true}} \sim 0\,\text{m s}^{-1}$. For the shortest data input time interval considered ($\Delta t = 5$ s), (18) yields the first spurious modes ($m = \pm 1$) as $V \sim V_{\text{true}} \pm 100\,\text{m s}^{-1}$, which we suspect will not be retrieved as long as reasonable first guesses for V are used. On the other hand, for the longest data input time interval considered ($\Delta t = 30$ s), the first spurious modes $V \sim V_{\text{true}} \pm 17\,\text{m s}^{-1}$ may be problematic.

By examining contour plots of $J(U, V)$ using advection-corrected data on subdomain boxes in the RFD, we confirmed that the nonuniqueness threat is largely absent when data of high time resolution ($\Delta t = 5$ s) are used but present when data of coarse time resolution ($\Delta t = 30$ s) are used.[7] A representative plot is shown in Fig. 14 for the same subdomain box shown in Fig. 13. In the $\Delta t = 5$-s panel, both the global minimum in J and a weak secondary minimum in J close to the global minimum correspond to the strong RFD northerlies. In the panel for $\Delta t = 30$ s, the northerlies are somewhat subdued, corresponding to a local minimum at $U \approx -3\,\text{m s}^{-1}$, $V \approx -18\,\text{m s}^{-1}$. Of more concern, however, is a spurious local minimum at $U \approx 0\,\text{m s}^{-1}$, $V \approx -4\,\text{m s}^{-1}$, consistent with the $m = 1$ aliased solution. A particularly disturbing aspect of this local minimum is that it is also the global minimum and, thus, would win out in a scheme that identified the "solution" as the global minimum of a set of candidate local minima. Additionally, a third minimum in J is hiding in the diffuse pink "tail" in the upper part of the panel. Zooming in on this part of the figure and changing the color scheme reveals a subtle minimum at $U \approx 4\,\text{m s}^{-1}$, $V \approx 13\,\text{m s}^{-1}$ (Fig. 15), which is likely a manifestation of the $m = 2$ spurious mode. Other J plots in the RFD constructed using the same 30-s data input time interval but different box sizes reveal similar patterns of multiminima, with the various minima switching prominence.

Presumably the danger posed by multiminima in $J(U, V)$ on analysis subdomains in the RFD for large Δt depends, in part, on the nature of the first guesses used. For instance, in the AC-GC1 experiments, where the first guess for U and V (mean u and v) is close to the "correct" local minimum (strong northerlies), the iterative procedure for U and V might be less likely to converge to a spurious minimum than in the multiguess

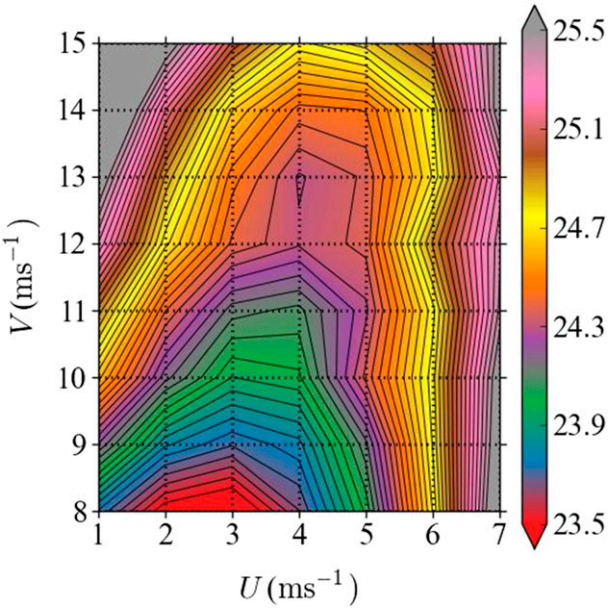

FIG. 15. Closeup view of the $\Delta t = 30$-s $J(U, V)$ field ($\text{m}^4\,\text{s}^{-3} \times 10^3$) of Fig. 14.

AC-GC9 experiments, where a first guess is in the vicinity of at least one spurious minimum, and there is no guarantee (or reason to expect) that the global minimum would be the correct minimum. The V fields retrieved in AC-GC1 using 1.2-km-wide subdomain boxes are shown in Fig. 16. With use of the higher-time-resolution data ($\Delta t = 5$ s), the retrieved V field was dominated by a pattern of strong northerlies over the northwestern half of the domain, which was consistent with the pattern of northerlies in the v field (Fig. 6). When the coarser-time-resolution data ($\Delta t = 30$ s) were used, the broad zone of strong V northerlies, though still present, was peppered with boxes of weak V northerlies ($m = 1$ aliased solution), zero values of V (indicating nonconvergence of the procedure), and even a few V southerlies (associated with the $m = 2$ aliased solution). However, as can be seen in Fig. 17, the threat of multiminima was much more fully realized in experiment AC-GC9, where aliased values of V obliterated large regions of the RFD.

For completeness, we also show the U field retrieved in AC-GC1 using the 1.2-km-wide subdomain boxes (Fig. 18). The patterns obtained with $\Delta t = 5$ and 30 s are qualitatively similar, though with the less cohesive patterns in the $\Delta t = 30$-s experiment suggestive of a multiminima problem, as in the V field results. For the $\Delta t = 5$-s experiment, the U field in the northwestern half of the domain is fairly consistent with the u field (Fig. 6). However, there are significant differences between the U and u fields in the southeastern half of the domain, particularly in the region of strong inflow, where u is

[7] We evaluated $J(U, V)$ by brute force—that is, by explicitly evaluating (4) for a large range of imposed U and V values. Each imposed pair of U and V values was used to advection correct u and v, which were then used in (4). The U and V values were specified in $1\,\text{m s}^{-1}$ increments.

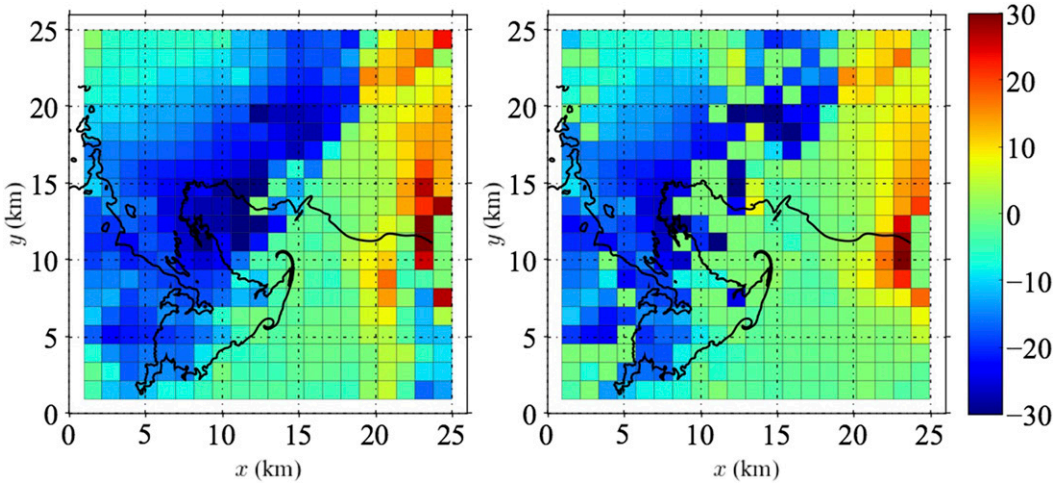

FIG. 16. Checkerboard plots of V (m s^{-1}) from experiments AC-GC1 run on 1.2-km-wide subdomain boxes using data at time intervals (left) 5 and (right) 30 s. Solid black curve marks the 40-dBZ model-equivalent radar reflectivity contour.

characterized by strong easterlies ($u \sim -25$ m s^{-1}) but U is close to 0 m s^{-1}. Here, the u pattern appeared smooth and laminar, with plots of u at other times throughout the 5-min integration window (not shown) suggesting the pattern was relatively stationary. Since the V field in this strong inflow region was also very weak, we infer that the velocity field in this region tended to move with the storm.

The J plots shown in Fig. 19 for a subdomain box in the inflow region reveals a single minimum in J near the origin (i.e., in the correct location) for both $\Delta t = 5$ and 30 s. Accordingly, the Gal-Chen procedure should yield the correct solution for any first-guess U–V pair, as long as the procedure converges. In contrast, since the box-averaged wind field (specifically, the u component) differs substantially from the pattern motion in this region, the AC-MW experiments would likely have large errors in this region. These disparate results are confirmed in Figs. 10 and 12.

5. Summary

Our study suggests that judicious use of an advection correction procedure can reduce errors in trajectory calculations associated with the temporal interpolation step. We explored use of an iterative technique originally proposed by Gal-Chen to reduce errors in radar data analyses associated with nonsimultaneity of the data collection. Two first-guess options for the U–V pattern-translation components were tested: use of a single U–V pair defined by the local mean winds (winds averaged on analysis subdomain boxes) and use of an array of multiple first guesses for U and V. In tests using a high-resolution simulated supercell dataset, use of the Gal-Chen procedure with either first-guess option yielded superior results to the traditional linear time interpolation procedure for all data input time intervals and all subdomain box sizes considered. The Gal-Chen procedure also proved superior to directly using local mean-wind estimates as the pattern-translation components, although there were large areas of the RFD where this latter approach worked quite well.

However, despite the encouraging results, the specter of solution nonuniqueness (multiminima in the cost-function

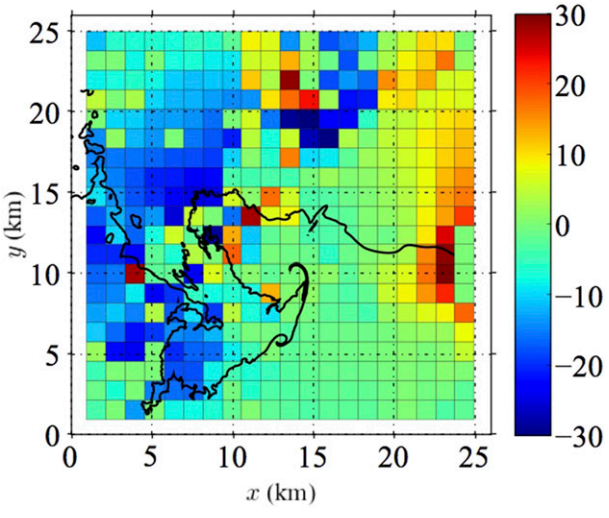

FIG. 17. Checkerboard plot of V (m s^{-1}) from experiment AC-GC9 run on 1.2-km-wide subdomain boxes using data at time intervals of $\Delta t = 30$ s. Solid black curve marks the 40-dBZ model-equivalent radar reflectivity contour.

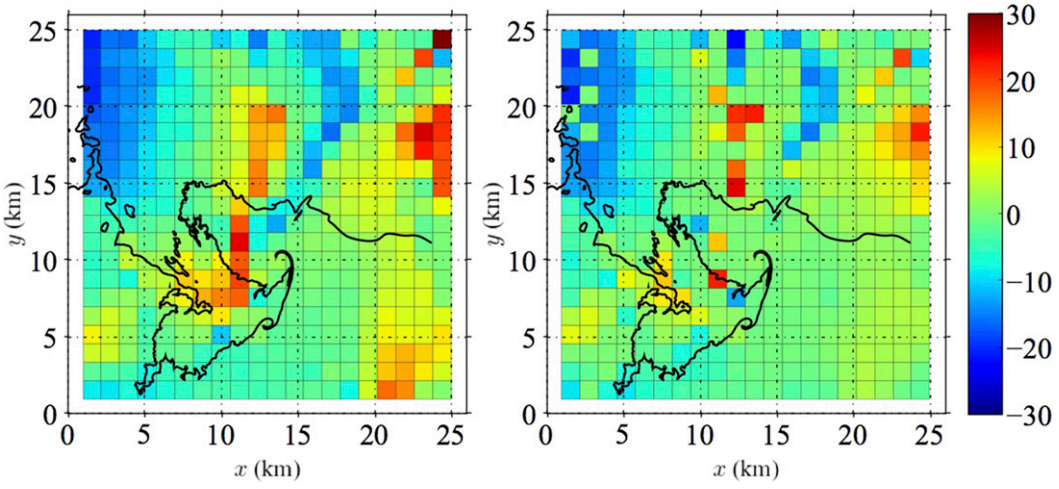

FIG. 18. As in Fig. 16, but for U.

J underlying the estimation of U and V) hung over the Gal-Chen procedure when the time resolution was too coarse. The nonuniqueness was associated with temporal aliasing, a known side effect of the Gal-Chen procedure and related pattern-tracking algorithms (Shapiro et al. 2010). In the coarse-time-resolution tests, aliasing became significant in the RFD, where small-scale wavy disturbances moved with the prevailing winds. Moreover, in this region, the global minimum in J could not be relied on to represent the correct (physical) solution. Accordingly, in this region, use of a single first-guess U–V pair defined by the local mean-wind components was preferable

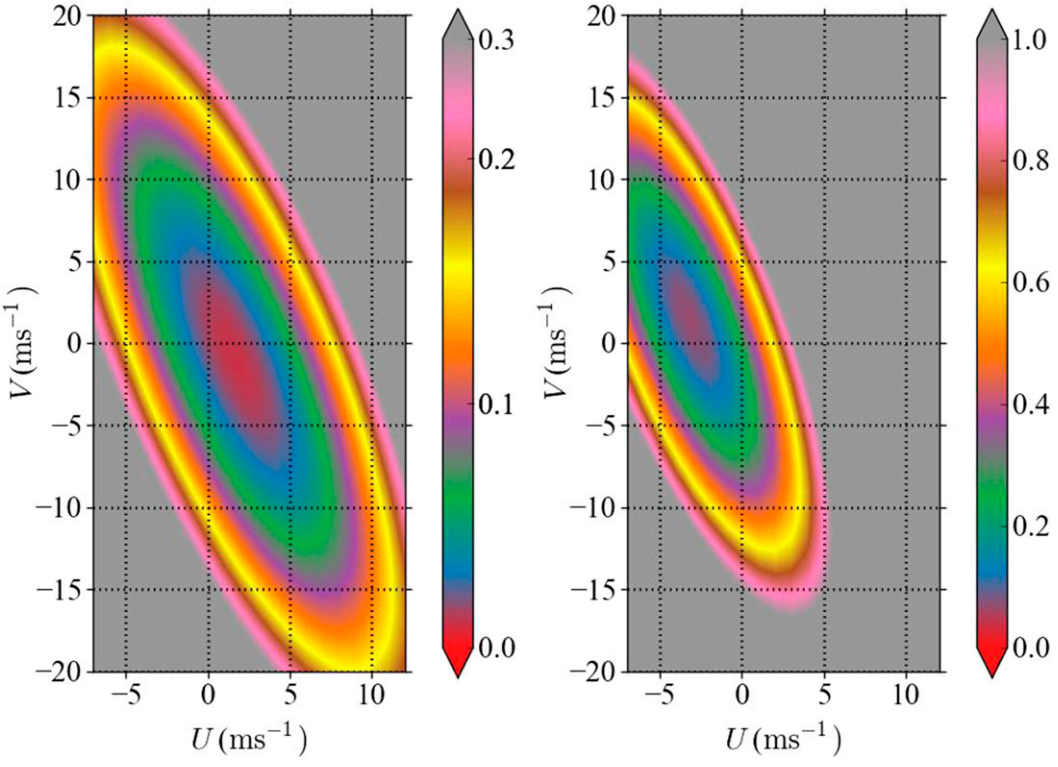

FIG. 19. Plots of $J(U, V)$ ($m^4\ s^{-3} \times 10^3$) for a 3.3-km-wide subdomain box located in the inflow region constructed using data at time intervals of (left) 5 and (right) 30 s. The southwestern corner of the box is at $x \approx 13.2$ km, $y \approx 9.9$ km. Data were used at times $t = 6650$ s and either $t = 6555$ s ($\Delta t = 5$ s) or $t = 6580$ s ($\Delta t = 30$ s).

to use of multiple first guesses. In contrast, analysis subdomains in the inflow region were characterized by unique solutions, and the Gal-Chen procedure yielded unique (and correct) solutions there regardless of the first-guess option. Use of a single first-guess U–V pair based on the local mean wind was therefore the overall preferred method. However, our recommendation to use such a first guess in general is tentative since our experiments were only performed with one dataset. Alternatively, in cases where a nonuniqueness threat has been identified (e.g., through analysis of J plots or use of multiple first guesses), one may forego the advection correction step and simply default to linear time interpolation.

Although the two-dimensional framework facilitated our exploration of advection correction in trajectory calculations, we recognize that three-dimensional procedures will be essential for most applications. The advection correction steps in section 2 can be extended to three dimensions by calculating U and V level by level and advection-correcting u and v level by level. Alternatively, one may obtain U and V, and a vertical translation component W by minimizing a three-dimensional version of (4), as in Zhang and Gal-Chen (1996) (though with J based on u and/or v instead of reflectivity). In this case, setting $\partial J/\partial U = \partial J/\partial V = \partial J/\partial W = 0$ yields three linear algebraic equations that are readily solved for U, V, and W. Once the pattern-translation components have been determined (by any method), it is straightforward to translate the virtual particles, spatially interpolate the velocity data to the particles' locations at the data input times, and perform the trajectory integrations using three-dimensional procedures.

Acknowledgments. We thank Jim Marquis, David Parsons, and the anonymous reviewers for their helpful comments.

REFERENCES

Adlerman, E. J., K. K. Droegemeier, and R. Davies-Jones, 1999: A numerical simulation of cyclic mesocyclogenesis. *J. Atmos. Sci.*, **56**, 2045–2069, doi:10.1175/1520-0469(1999)056<2045:ANSOCM>2.0.CO;2.

Anagnostou, E. N., and W. F. Krajewski, 1999: Real-time radar rainfall estimation. Part I: Algorithm formulation. *J. Atmos. Oceanic Technol.*, **16**, 189–197, doi:10.1175/1520-0426(1999)016<0189:RTRREP>2.0.CO;2.

Baker, J., 2010: Cluster analysis of long range air transport pathways and associated pollutant concentrations within the UK. *Atmos. Environ.*, **44**, 563–571, doi:10.1016/j.atmosenv.2009.10.030.

Beckie, H. J., and L. M. Hall, 2008: Simple to complex: Modelling crop pollen-mediated gene flow. *Plant Sci.*, **175**, 615–628, doi:10.1016/j.plantsci.2008.05.021.

Belmonte, J., M. Alarcón, A. Avila, E. Scialabba, and D. Pino, 2008: Long-range transport of beech (*Fagus sylvatica* L.) pollen to Catalonia (north-eastern Spain). *Int. J. Biometeorol.*, **52**, 675–687, doi:10.1007/s00484-008-0160-9.

Blanke, B., and S. Raynaud, 1997: Kinematics of the Pacific Equatorial Undercurrent: An Eulerian and Lagrangian approach from GCM results. *J. Phys. Oceanogr.*, **27**, 1038–1053, doi:10.1175/1520-0485(1997)027<1038:KOTPEU>2.0.CO;2.

Bluestein, H. B., and S. G. Gaddy, 2001: Airborne pseudo-dual-Doppler analysis of a rear-inflow jet and deep convergence zone within a supercell. *Mon. Wea. Rev.*, **129**, 2270–2289, doi:10.1175/1520-0493(2001)129<2270:APDDAO>2.0.CO;2.

Brandes, E. A., 1981: Finestructure of the Del City-Edmond tornadic mesocirculation. *Mon. Wea. Rev.*, **109**, 635–647, doi:10.1175/1520-0493(1981)109<0635:FOTDCE>2.0.CO;2.

——, 1984: Relationships between radar-derived thermodynamic variables and tornadogenesis. *Mon. Wea. Rev.*, **112**, 1033–1052, doi:10.1175/1520-0493(1984)112<1033:RBRDTV>2.0.CO;2.

Brankov, E., S. T. Rao, and P. S. Porter, 1998: A trajectory-clustering-correlation methodology for examining the long-range transport of air pollutants. *Atmos. Environ.*, **32**, 1525–1534, doi:10.1016/S1352-2310(97)00388-9.

Breivik, Ø., and A. A. Allen, 2008: An operational search and rescue model for the Norwegian Sea and the North Sea. *J. Mar. Syst.*, **69**, 99–113, doi:10.1016/j.jmarsys.2007.02.010.

Bryan, G. H., and H. Morrison, 2012: Sensitivity of a simulated squall line to horizontal resolution and parameterization of microphysics. *Mon. Wea. Rev.*, **140**, 202–225, doi:10.1175/MWR-D-11-00046.1.

Buchanan, C. M., I. J. Beverland, and M. R. Heal, 2002: The influence of weather-type and long-range transport on airborne particle concentrations in Edinburgh, UK. *Atmos. Environ.*, **36**, 5343–5354, doi:10.1016/S1352-2310(02)00579-4.

Cabezudo, B., M. Recio, J.-M. Sánchez-Laulhé, M. M. Trigo, F. J. Toro, and F. Polvorinos, 1997: Atmospheric transportation of marihuana pollen from North Africa to the southwest of Europe. *Atmos. Environ.*, **31**, 3323–3328, doi:10.1016/S1352-2310(97)00161-1.

Carbone, R. E., 1982: A severe frontal rainband. Part I: Storm-wide hydrodynamic structure. *J. Atmos. Sci.*, **39**, 258–279, doi:10.1175/1520-0469(1982)039<0258:ASFRPI>2.0.CO;2.

Chapra, S. C., and R. P. Canale, 2005: *Numerical Methods for Engineers.* 5th ed. McGraw Hill, 926 pp.

Chong, M., J. Testud, and F. Roux, 1983: Three-dimensional wind field analysis from dual-Doppler radar data. Part II: Minimizing the error due to temporal variation. *J. Climate Appl. Meteor.*, **22**, 1216–1226, doi:10.1175/1520-0450(1983)022<1216:TDWFAF>2.0.CO;2.

Chu, P. C., and C. Fan, 2014: Accuracy progressive calculation of Lagrangian trajectories from a gridded velocity field. *J. Atmos. Oceanic Technol.*, **31**, 1615–1627, doi:10.1175/JTECH-D-13-00204.1.

Ciach, G. J., W. F. Krajewski, E. N. Anagnostou, M. L. Baeck, J. A. Smith, J. R. McCollum, and A. Kruger, 1997: Radar rainfall estimation for ground validation studies of the Tropical Rainfall Measuring Mission. *J. Appl. Meteor.*, **36**, 735–747, doi:10.1175/1520-0450-36.6.735.

Cifelli, R., W. A. Petersen, L. D. Carey, S. A. Rutledge, and M. A. F. da Silva Dias, 2002: Radar observations of the kinematic, microphysical, and precipitation characteristics of two MCSs in TRMM LBA. *J. Geophys. Res.*, **107**, 8077, doi:10.1029/2000JD000264.

Courant, R., 1988: *Differential and Integral Calculus.* Vol. II. Wiley-Interscience, 682 pp.

D'Abreton, P. C., and P. D. Tyson, 1996: Three-dimensional kinematic trajectory modelling of water vapour transport over southern Africa. *Water SA*, **22**, 297–306.

Dahl, J. M. L., M. D. Parker, and L. J. Wicker, 2012: Uncertainties in trajectory calculations within near-surface mesocyclones of simulated supercells. *Mon. Wea. Rev.*, **140**, 2959–2966, doi:10.1175/MWR-D-12-00131.1.

——, ——, and ——, 2014: Imported and storm-generated near-ground vertical vorticity in a simulated supercell. *J. Atmos. Sci.*, **71**, 3027–3051, doi:10.1175/JAS-D-13-0123.1.

Davies-Jones, R. P., and H. E. Brooks, 1993: Mesocyclogenesis from a theoretical perspective. *The Tornado: Its Structure, Dynamics, Prediction and Hazards, Geophys. Monogr.*, Vol. 79, Amer. Geophys. Union, 105–114.

Dawson, D. T., M. Xue, J. A. Milbrandt, and M. K. Yau, 2010: Comparison of evaporation and cold pool development between single-moment and multimoment bulk microphysics schemes in idealized simulations of tornadic thunderstorms. *Mon. Wea. Rev.*, **138**, 1152–1171, doi:10.1175/2009MWR2956.1.

Dayan, U., 1986: Climatology of back trajectories from Israel based on synoptic analysis. *J. Climate Appl. Meteor.*, **25**, 591–595, doi:10.1175/1520-0450(1986)025<0591:COBTFI>2.0.CO;2.

Doty, K. G., and D. J. Perkey, 1993: Sensitivity of trajectory calculations to the temporal frequency of wind data. *Mon. Wea. Rev.*, **121**, 387–401, doi:10.1175/1520-0493(1993)121<0387:SOTCTT>2.0.CO;2.

Dowell, D. C., and H. B. Bluestein, 1997: The Arcadia, Oklahoma, storm of 17 May 1981: Analysis of a supercell during tornadogenesis. *Mon. Wea. Rev.*, **125**, 2562–2582, doi:10.1175/1520-0493(1997)125<2562:TAOSOM>2.0.CO;2.

——, and ——, 2002: The 8 June 1995 McLean, Texas storm. Part II: Cyclic tornado formation, maintenance, and dissipation. *Mon. Wea. Rev.*, **130**, 2649–2670, doi:10.1175/1520-0493(2002)130<2649:TJMTSP>2.0.CO;2.

Engelstaedter, S., I. Tegen, and R. Washington, 2006: North African dust emissions and transport. *Earth-Sci. Rev.*, **79**, 73–100, doi:10.1016/j.earscirev.2006.06.004.

Fabry, F., A. Bellon, M. R. Duncan, and G. L. Austin, 1994: High resolution rainfall measurements by radar for very small basins: The sampling problem reexamined. *J. Hydrol.*, **161**, 415–428, doi:10.1016/0022-1694(94)90138-4.

Frame, J., P. Markowski, Y. Richardson, J. Straka, and J. Wurman, 2009: Polarimetric and dual-Doppler radar observations of the Lipscomb County, Texas, supercell thunderstorm on 23 May 2002. *Mon. Wea. Rev.*, **137**, 544–561, doi:10.1175/2008MWR2425.1.

Gal-Chen, T., 1982: Errors in fixed and moving frame of references: Applications for conventional and Doppler radar analysis. *J. Atmos. Sci.*, **39**, 2279–2300, doi:10.1175/1520-0469(1982)039<2279:EIFAMF>2.0.CO;2.

Griffa, A., L. I. Piterbarg, and T. Özgökmen, 2004: Predictability of Lagrangian particle trajectories: Effects of smoothing of the underlying Eulerian flow. *J. Mar. Res.*, **62**, 1–35, doi:10.1357/002224004460744609.

Harris, J. M., R. R. Draxler, and S. J. Oltmans, 2005: Trajectory model sensitivity to differences in input data and vertical transport method. *J. Geophys. Res.*, **110**, D14109, doi:10.1029/2004JD005750.

Hjelmroos, M., 1991: Evidence of long-distance transport of Betula pollen. *Grana*, **30**, 215–228, doi:10.1080/00173139109427802.

Ioannidou, A., and Coauthors, 2013: An air-mass trajectory study of the transport of radioactivity from Fukushima to Thessaloniki, Greece and Milan, Italy. *Atmos. Environ.*, **75**, 163–170, doi:10.1016/j.atmosenv.2013.04.008.

Johnson, K. W., P. S. Ray, B. C. Johnson, and R.-P. Davies Jones, 1987: Observations related to the rotational dynamics of the 20 May 1977 tornadic storms. *Mon. Wea. Rev.*, **115**, 2463–2478, doi:10.1175/1520-0493(1987)115<2463:ORTTRD>2.0.CO;2.

Kahl, J. D., and P. J. Samson, 1986: Uncertainty in trajectory calculations due to low resolution meteorological data. *J. Climate Appl. Meteor.*, **25**, 1816–1831, doi:10.1175/1520-0450(1986)025<1816:UITCDT>2.0.CO;2.

——, D. A. Martinez, H. Kuhns, C. I. Davidson, J.-L. Jaffrezo, and J. M. Harris, 1997: Air mass trajectories to Summit, Greenland: A 44-year climatology and some episodic events. *J. Geophys. Res.*, **102**, 26 861–26 875, doi:10.1029/97JC00296.

Knippertz, P., and H. Wernli, 2010: A Lagrangian climatology of tropical moisture exports to the Northern Hemispheric extratropics. *J. Climate*, **23**, 987–1003, doi:10.1175/2009JCLI3333.1.

Kosiba, K. A., and J. Wurman, 2014: Finescale dual-Doppler analysis of hurricane boundary layer structures in Hurricane Frances (2004) at landfall. *Mon. Wea. Rev.*, **142**, 1874–1891, doi:10.1175/MWR-D-13-00178.1.

——, ——, Y. Richardson, P. Markowski, P. Robinson, and J. Marquis, 2013: Genesis of the Goshen County, Wyoming, tornado on 5 June 2009 during VORTEX2. *Mon. Wea. Rev.*, **141**, 1157–1181, doi:10.1175/MWR-D-12-00056.1.

Kundu, P. K., 1990: *Fluid Mechanics.* Academic Press, 638 pp.

Kuo, Y.-H., M. Skumanich, P. L. Haagenson, and J. S. Chang, 1985: The accuracy of trajectory models as revealed by the observing system simulation experiments. *Mon. Wea. Rev.*, **113**, 1852–1867, doi:10.1175/1520-0493(1985)113<1852:TAOTMA>2.0.CO;2.

Kuparinen, A., F. Schurr, O. Tackenberg, and R. B. O'Hara, 2007: Air-mediated pollen flow from genetically modified to conventional crops. *Ecol. Appl.*, **17**, 431–440, doi:10.1890/05-1599.

Liu, S., C. Qiu, and Q. Xu, 2004: An improved time interpolation for three-dimensional Doppler wind analysis. *J. Appl. Meteor.*, **43**, 1379–1391, doi:10.1175/JAM2150.1.

Liu, Y., R. H. Weisberg, C. Hu, and L. Zheng, 2011: Trajectory forecast as a rapid response to the Deepwater Horizon oil spill. *Monitoring and Modeling the Deepwater Horizon Oil Spill: A Record-Breaking Enterprise. Geophys. Monogr.*, Vol. 195, Amer. Geophys. Union, 153–165.

Marquis, J., Y. Richardson, J. Wurman, and P. Markowski, 2008: Single- and dual-Doppler analysis of a tornadic vortex and surrounding storm-scale flow in the Crowell, Texas, supercell of 30 April 2000. *Mon. Wea. Rev.*, **136**, 5017–5043, doi:10.1175/2008MWR2442.1.

——, ——, P. Markowski, D. Dowell, and J. Wurman, 2012: Tornado maintenance investigated with high-resolution dual-Doppler and EnKF analysis. *Mon. Wea. Rev.*, **140**, 3–27, doi:10.1175/MWR-D-11-00025.1.

——, ——, ——, ——, ——, K. Kosiba, P. Robinson, and G. Romine, 2014: An investigation of the Goshen County, Wyoming, tornadic supercell of 5 June 2009 using EnKF assimilation of mobile mesonet and radar observations collected during VORTEX2. Part I: Experiment design and verification of the EnKF analyses. *Mon. Wea. Rev.*, **142**, 530–554, doi:10.1175/MWR-D-13-00007.1.

Melsom, A., F. Counillon, J. H. LaCasce, and L. Bertino, 2012: Forecasting search areas using ensemble ocean circulation modeling. *Ocean Dyn.*, **62**, 1245–1257, doi:10.1007/s10236-012-0561-5.

Miller, J. M., 1981: A five-year climatology of back trajectories from the Mauna Loa Observatory, Hawaii. *Atmos. Environ.*, **15**, 1553–1558, doi:10.1016/0004-6981(81)90138-4.

Miltenberger, A. K., S. Pfahl, and H. Wernli, 2013: An online trajectory module (version 1.0) for the nonhydrostatic numerical weather prediction model COSMO. *Geosci. Model Dev.*, **6**, 1989–2004, doi:10.5194/gmd-6-1989-2013.

Moody, J. L., S. J. Oltmans, H. Levy, and J. T. Merrill, 1995: Transport climatology of tropospheric ozone: Bermuda, 1981–1991. *J. Geophys. Res.*, **100**, 7179–7194, doi:10.1029/94JD02830.

Naylor, J., and M. S. Gilmore, 2014: Vorticity evolution leading to tornadogenesis and tornadogenesis failure in simulated supercells. *J. Atmos. Sci.*, **71**, 1201–1217, doi:10.1175/JAS-D-13-0219.1.

Nielsen, J. E., S. Thorndahl, and M. R. Rasmussen, 2014: A numerical method to generate high temporal resolution precipitation time series by combining weather radar measurements with a nowcast model. *Atmos. Res.*, **138**, 1–12, doi:10.1016/j.atmosres.2013.10.015.

Orf, L., R. Wilhelmson, and L. Wicker, 2014: Numerical simulation of a supercell with an embedded long-track EF5 tornado. *Special Symp. on Severe Local Storms: The Current State of the Science and Understanding Impacts*, Atlanta, GA, Amer. Meteor. Soc., P815. [Available online at https://ams.confex.com/ams/94Annual/webprogram/Paper242579.html.]

Park, S. K., M. S. O'Neill, B. J. B. Stunder, P. S. Vokonas, D. Sparrow, P. Koutrakis, and J. Schwartz, 2007: Source location of air pollution and cardiac autonomic function: Trajectory cluster analysis for exposure assessment. *J. Exposure Sci. Environ. Epidemiol.*, **17**, 488–497, doi:10.1038/sj.jes.7500552.

Pöllänen, R., I. Valkama, and H. Toivonen, 1997: Transport of radioactive particles from the Chernobyl accident. *Atmos. Environ.*, **31**, 3575–3590, doi:10.1016/S1352-2310(97)00156-8.

Potvin, C. K., L. J. Wicker, D. Betten, M. I. Biggerstaff, and A. Shapiro, 2013: Comparison between dual-Doppler and EnKF storm-scale wind analyses: The 29–30 May 2004 Geary, Oklahoma, supercell thunderstorm. *Mon. Wea. Rev.*, **141**, 1612–1628, doi:10.1175/MWR-D-12-00308.1.

Povinec, P. P., I. Sýkora, M. Gera, K. Holý, L. Brest'áková, and A. Kováčik, 2013: Fukushima-derived radionuclides in ground-level air of Central Europe: A comparison with simulated forward and backward trajectories. *J. Radioanal. Nucl. Chem.*, **295**, 1171–1176, doi:10.1007/s10967-012-1943-3.

Price, J. M., M. Reed, M. K. Howard, W. R. Johnson, Z.-G. Ji, C. F. Marshall, N. L. Guinasso Jr., and G. B. Rainey, 2006: Preliminary assessment of an oil-spill trajectory model using satellite-tracked, oil-spill-simulating drifters. *Environ. Modell. Software*, **21**, 258–270, doi:10.1016/j.envsoft.2004.04.025.

Rantio-Lehtimäki, A., 1994: Short, medium and long range transported airborne particles in viability and antigenicity analyses. *Aerobiologia*, **10**, 175–181, doi:10.1007/BF02459233.

Riddle, E. E., P. B. Voss, A. Stohl, D. Holcomb, D. Maczka, K. Washburn, and R. W. Talbot, 2006: Trajectory model validation using newly developed altitude-controlled balloons during the International Consortium for Atmospheric Research on Transport and Transformations 2004 campaign. *J. Geophys. Res.*, **111**, D23S57, doi:10.1029/2006JD007456.

Roberts, R. D., and J. W. Wilson, 1995: The genesis of three nonsupercell tornadoes observed with dual-Doppler radar. *Mon. Wea. Rev.*, **123**, 3408–3436, doi:10.1175/1520-0493(1995)123<3408:TGOTNT>2.0.CO;2.

Rolph, G. D., and R. R. Draxler, 1990: Sensitivity of three-dimensional trajectories to the spatial and temporal densities of the wind field. *J. Appl. Meteor.*, **29**, 1043–1054, doi:10.1175/1520-0450(1990)029<1043:SOTDTT>2.0.CO;2.

Rosenhead, L., Ed., 1963: *Laminar Boundary Layers*. Oxford University Press, 688 pp.

Rössler, C. E., T. Paccagnella, and St. Tibaldi, 1992: A three-dimensional atmospheric trajectory model: Application to a case study of Alpine lee cyclogenesis. *Meteor. Atmos. Phys.*, **50**, 211–229, doi:10.1007/BF01026018.

Rotunno, R., and J. Klemp, 1985: On the rotation and propagation of simulated supercell thunderstorms. *J. Atmos. Sci.*, **42**, 271–292, doi:10.1175/1520-0469(1985)042<0271:OTRAPO>2.0.CO;2.

Salathé, E. P., and D. L. Hartmann, 1997: A trajectory analysis of tropical upper-tropospheric moisture and convection. *J. Climate*, **10**, 2533–2547, doi:10.1175/1520-0442(1997)010<2533:ATAOTU>2.0.CO;2.

Sasaki, Y., 1970: Some basic formalisms in numerical variational analysis. *Mon. Wea. Rev.*, **98**, 875–883, doi:10.1175/1520-0493(1970)098<0875:SBFINV>2.3.CO;2.

Scheele, M. P., P. C. Siegmund, and P. F. J. van Velthoven, 1996: Sensitivity of trajectories to data resolution and its dependence on the starting point: In or outside a tropopause fold. *Meteor. Appl.*, **3**, 267–273, doi:10.1002/met.5060030308.

Schenkman, A. D., 2012: Exploring tornadogenesis with high-resolution simulations initialized with real data. Ph.D. dissertation, University of Oklahoma, 186 pp.

——, M. Xue, and A. Shapiro, 2012: Tornadogenesis in a simulated mesovortex within a mesoscale convective system. *J. Atmos. Sci.*, **69**, 3372–3390, doi:10.1175/JAS-D-12-038.1.

——, ——, and M. Hu, 2014: Tornadogenesis in a high-resolution simulation of the 8 May 2003 Oklahoma City supercell. *J. Atmos. Sci.*, **71**, 130–154, doi:10.1175/JAS-D-13-073.1.

Seibert, P., 1993: Convergence and accuracy of numerical methods for trajectory calculations. *J. Appl. Meteor.*, **32**, 558–566, doi:10.1175/1520-0450(1993)032<0558:CAAONM>2.0.CO;2.

Shadboldt, R. P., E. A. Waller, J. P. Messina, and J. A. Winkler, 2006: Source regions of lower-tropospheric airflow trajectories for the lower peninsula of Michigan: A 40-year air mass climatology. *J. Geophys. Res.*, **111**, D21117, doi:10.1029/2005JD006657.

Shapiro, A., K. M. Willingham, and C. K. Potvin, 2010: Spatially variable advection correction of radar data. Part I: Theoretical considerations. *J. Atmos. Sci.*, **67**, 3445–3456, doi:10.1175/2010JAS3465.1.

Smith, M., and Coauthors, 2008: Long-range transport of *Ambrosia* pollen to Poland. *Agric. For. Meteor.*, **148**, 1402–1411, doi:10.1016/j.agrformet.2008.04.005.

Sotillo, M. G., and Coauthors, 2008: Towards an operational system for oil-spill forecast over Spanish waters: Initial developments and implementation test. *Mar. Pollut. Bull.*, **56**, 686–703, doi:10.1016/j.marpolbul.2007.12.021.

Spaulding, M. L., 1988: A state-of-the-art review of oil spill trajectory and fate modeling. *Oil Chem. Pollut.*, **4**, 39–55, doi:10.1016/S0269-8579(88)80009-1.

Stach, A., M. Smith, C. A. Skjøth, and J. Brandt, 2007: Examining *Ambrosia* pollen episodes at Poznań (Poland) using back-trajectory analysis. *Int. J. Biometeor.*, **51**, 275–286, doi:10.1007/s00484-006-0068-1.

Stohl, A., 1996: Trajectory statistics: A new method to establish source-receptor relationships of air pollutants and its application to the transport of particulate sulfate in Europe. *Atmos. Environ.*, **30**, 579–587, doi:10.1016/1352-2310(95)00314-2.

——, 1998: Computation, accuracy and applications of trajectories—A review and bibliography. *Atmos. Environ.*, **32**, 947–966, doi:10.1016/S1352-2310(97)00457-3.

——, and H. Kromp-Kolb, 1994: Origin of ozone in Vienna and surroundings, Austria. *Atmos. Environ.*, **28**, 1255–1266, doi:10.1016/1352-2310(94)90272-0.

——, and P. Seibert, 1998: Accuracy of trajectories determined from the conservation of meteorological tracers. *Quart. J. Roy. Meteor. Soc.*, **124**, 1465–1484, doi:10.1002/qj.49712454907.

——, G. Wotawa, P. Seibert, and H. Kromp-Kolb, 1995: Interpolation errors in wind fields as a function of spatial and temporal resolution and their impact on different types of kinematic trajectories. *J. Appl. Meteor.*, **34**, 2149–2165, doi:10.1175/1520-0450(1995)034<2149:IEIWFA>2.0.CO;2.

——, L. Haimberger, M. P. Scheele, and H. Wernli, 2001: An intercomparison of results from three trajectory models. *Meteor. Appl.*, **8**, 127–135, doi:10.1017/S1350482701002018.

Sturman, A., and P. Zawar-Reza, 2002: Application of back-trajectory techniques to the delimitation of urban clean air zones. *Atmos. Environ.*, **36**, 3339–3350, doi:10.1016/S1352-2310(02)00253-4.

Tabary, P., 2007: The new French operational radar rainfall product. Part I: Methodology. *Wea. Forecasting*, **22**, 393–408, doi:10.1175/WAF1004.1.

Taylor, G. I., 1938: The spectrum of turbulence. *Proc. Roy. Soc. London*, **164A**, 476–490.

Van de Water, P. K., L. S. Watrud, E. H. Lee, C. Burdick, and G. A. King, 2007: Long-distance GM pollen movement of creeping bentgrass using modeled wind trajectory analysis. *Ecol. Appl.*, **17**, 1244–1256, doi:10.1890/06-0962.

Villarini, G., and W. F. Krajewski, 2010: Review of the different sources of uncertainty in single-polarization radar-based estimates of rainfall. *Surv. Geophys.*, **31**, 107–129, doi:10.1007/s10712-009-9079-x.

Wakimoto, R. M., C. Liu, and H. Cai, 1998: The Garden City, Kansas, storm during VORTEX 95. Part I: Overview of the storm's lifecycle and mesocyclogenesis. *Mon. Wea. Rev.*, **126**, 372–392, doi:10.1175/1520-0493(1998)126<0372:TGCKSD>2.0.CO;2.

Wernli, H., and H. C. Davies, 1997: A Lagrangian-based analysis of extratropical cyclones. I: The method and some applications. *Quart. J. Roy. Meteor. Soc.*, **123**, 467–489, doi:10.1002/qj.49712353811.

Wurman, J., Y. Richardson, C. Alexander, S. Weygandt, and P. F. Zhang, 2007: Dual-Doppler analysis of winds and vorticity budget terms near a tornado. *Mon. Wea. Rev.*, **135**, 2392–2405, doi:10.1175/MWR3404.1.

Xu, Q., X. Li, Y. Wei, Z. Tang, Y. Cheng, and W. G. Pichel, 2013: Satellite observations and modeling of oil spill trajectories in the Bohai Sea. *Mar. Pollut. Bull.*, **71**, 107–116, doi:10.1016/j.marpolbul.2013.03.028.

Zhang, J., and T. Gal-Chen, 1996: Single-Doppler wind retrieval in the moving frame of reference. *J. Atmos. Sci.*, **53**, 2609–2623, doi:10.1175/1520-0469(1996)053<2609:SDWRIT>2.0.CO;2.

Ziegler, C. L., E. N. Rasmussen, T. R. Shepherd, A. I. Watson, and J. M. Straka, 2001: The evolution of low-level rotation in the 29 May 1994 Newcastle-Graham, Texas, storm complex during VORTEX. *Mon. Wea. Rev.*, **129**, 1339–1368, doi:10.1175/1520-0493(2001)129<1339:TEOLLR>2.0.CO;2.